IEEE Access
Multidisciplinary | Rapid Review | Open Access Journal

Received October 28, 2018, accepted December 24, 2018, date of publication January 10, 2019, date of current version February 27, 2019.

Digital Object Identifier 10.1109/ACCESS.2019.2891952

Safety-Enhanced Model-Free Visual Servoing for Continuum Tubular Robots Through Singularity Avoidance in Confined Environments

KEYU WU[1], GUONIU ZHU[1], LIAO WU[1], WENCHAO GAO[1], SHUANG SONG[2], CHWEE MING LIM[3], AND HONGLIANG REN[1], (Senior Member, IEEE)

[1]Department of Biomedical Engineering, National University of Singapore, Singapore 119077
[2]School of Mechanical Engineering and Automation, Harbin Institute of Technology Shenzhen Graduate School, Shenzhen 518055, China
[3]Department of Otolaryngology, Head and Neck Surgery, National University Health System, Singapore 119228

Corresponding author: Hongliang Ren (hlren@ieee.org; ren@nus.edu.sg)

This work is supported by the Singapore NMRC Bedside & Bench under grant R-397-000-245-511 awarded to Dr. Hongliang Ren.

ABSTRACT Minimally invasive procedures have gained ever-increasing popularity due to their advantages of smaller incisions, faster recoveries, fewer complications, and reduced scarring to name a few. With the force exertion and curvilinear flexibility at their distal end effectors, the continuum tubular robots have the potential to perform robot-assisted trans-orifice minimally invasive surgery, such as transnasal and transoral operations. During these procedures, it is important and challenging for the continuum tubular robot to automatically adjust its pose according to the target surgical sites and compensate for undesired disturbance, such as respiratory motions. In this paper, a singularity-avoidance visual servoing algorithm based on Jacobian Optimization has been proposed to improve safety and control continuum tubular robots based on intra-operative visual feedback in confined environments. Without the prior knowledge of robot kinematics or hand-eye calibration between the robot and the endoscope, the proposed model-free eye-in-hand visual servoing technique is capable of accomplishing the targeting tasks by adopting the safety-enhanced singularity avoidance mechanism and an efficient image-processing algorithm. The multiple experiments, including simulations, experiments conducted in a confined environment, and cadaveric studies, have been implemented and demonstrated to illustrate the superiority of the proposed singularity-avoidance visual servoing method.

INDEX TERMS Visual servoing, singularity-avoidance, singularity-resistant, model-free, continuum tubular robots, concentric tube robots, image processing, minimally invasive surgery.

I. INTRODUCTION

Robot-assisted minimally invasive surgery has emerged as a new paradigm due to its potential to improve the performance of complex surgical procedures with higher precision and accuracy, as well as increased dexterity and stability, while minimizing trauma to the patient. However, intelligent and cooperative systems are urgently required to be integrated into more advanced surgical robots.

Continuum tubular robots (CTR), known as concentric tube robots, have been developed for minimally invasive surgery. This class of robots consists of several pre-curved elastic tubes that can rotate and translate independently [1]–[3] and their motion generations do not rely on tissue-robot interaction as a result of their relatively high stiffness. Because of the elastic deformation of each nesting tube, continuum tubular robots are capable of navigating through complex lumens to the target surgical sites, while bypassing critical anatomical obstacles. In addition, they can retain force transmission capability at the tooltip without loss of steering flexibility, which distinguishes them from tendon/cable driven flexible robots and makes them promising in quite a few trans-orifice minimally invasive surgeries [4]–[6].

A common mode to control continuum tubular robots is teleoperation, which establishes the mapping between robotic motion and movement of a master device [3], [7]. However, continuum tubular robots can only be roughly

The associate editor coordinating the review of this manuscript and approving it for publication was Cristian A. Linte.

guided to the desired surgical sites via teleoperation. More precise pose control and motion compensation ability are in demand to strengthen safety during robotic surgical manipulations. To this end, additional sensing ability is essential, including 3D ultrasound [8], X-ray [9], MRI [10], CT [11], fluoroscopy [12] and stereo optical imaging [13]–[15]. In addition, electromagnetic coils have been proposed to track the orientation and position of the tubular robots [16], or to reconstruct the shape of the robot body to achieve more precise pose control of flexible robots [17].

Direct vision-based methods, however, are the most advantageous approaches because less modification of the hardware is required, while accurate and reliable visual feedback is not compromised. Using image-based sensing techniques, measurements obtained from the visual feedback signals as the input to the robot control loop so that a visual servoing system can be constructed [18]–[20]. In addition, visual servoing is recognized to be an effective tool for physiological motion compensation [21], [22]. Nevertheless, quite a limited number of visual servoing algorithms are currently available for continuum tubular robots. Although a position-based visual servoing algorithm was proposed in [23], it was sensitive to calibration and reconstruction errors. Since image-based approaches do not require pose reconstruction of robots or hand-eye calibration, they are generally more robust to noises and disturbances [24], [25].

In literature, a significant amount of work is developing visual servoing approaches for robot control. A kinematics-based adaptive controller for image-based visual servoing was proposed to control the tip of the cable-driven manipulator by decreasing the errors of the feature points on the image plane [26], [27]. However, the algorithm was fairly complicated due to the involvement of the kinematics model and was only applicable in free space. Nevertheless, the majority of the resulting methods require prior knowledge of the system including kinematic structure and camera parameters. Using a model dependent system demands the calibration of the robot and vision system, or recalibration due to the sensitivity of the system to disturbances [28]–[30]. These activities can be both difficult and time-consuming, even unfeasible in a changing or complex environment. In a confined surgical environment, the model will be especially inaccurate because the constraints on the robot's configuration and the Jacobian cannot be effectively computed.

Therefore, a visual servoing controller that empirically estimates the image Jacobian online without a prior model is proposed in this paper. In order to avoid the aforementioned problems, a closed-loop feedback controller that empirically estimates the robot Jacobian online without any model was presented in [31]. This algorithm was only applied to the planar motion of an eye-to-hand system and was developed based on the properties of tendon-driven continuum robots instead of continuum tubular robots. Therefore, similar model-free mechanisms were introduced for continuum tubular robots to achieve both planar motions of an eye-to-hand system [32] and three-dimensional motion of eye-in-hand continuum tubular systems [33].

Although the aforementioned model-free visual servoing algorithms are well-functioning in free space, they are not stable when a singularity occurs in confined surgical environments. Generally, a singularity will lead the control performance to become divergent. Therefore, more advanced algorithms are in great need to prevent the system from being out of control due to the singularity of the Jacobian matrix [34]. In literature, many measures have been developed to predict and overcome the effects of singularity. For example, determinant based measures were proposed in [35], while they exhibited a wide range of numerical variation. Condition number based measures were then introduced because they were found to vary more smoothly over the workspace of PUMA and WAM. Hence, the condition number was regarded as the secondary task to optimize during the visual servoing process in [36], to avoid singularity of the Jacobian matrix.

However, the performance of the singularity avoidance algorithm mentioned above is not quite satisfactory when continuum tubular robots are adopted and modifications on the existing model-free visual servoing algorithm are required to ensure the safety and efficiency of manipulating eye-in-hand continuum tubular robotic systems. Therefore, a singularity-avoidance visual servoing algorithm is proposed in this paper to control the continuum tubular robot more reliably and efficiently in confined environments.

The main purpose of this paper is to deal with the singularity avoidance challenge for continuum tubular robots in confined environments. A singularity-resistant visual servoing algorithm based on Jacobian Optimization is proposed to address the singularity problem. Four image processing frameworks, including an intensity-based image processing algorithm, an intensity- and gradient-based image processing mechanism, and two saliency-based image processing methods are proposed and investigated as candidate image processing approaches. Multiple sets of experiments, including simulations, experiments conducted in a confined environment, and cadaveric studies, are carried out to evaluate the proposed singularity-avoidance visual servoing technique. The primary contribution of this paper include:

- A novel singularity-avoidance model-free eye-in-hand visual servoing technique is developed to achieve reliable and safe control over continuum tubular robots in confined surgical environments based on image feedback. A reliable singularity-resistant visual servoing algorithm based on Jacobian Optimization during the Jacobian update process is proposed to address the singularity avoidance challenge. The proposed visual servoing algorithm does not rely on any prior knowledge of the kinematic model of the robot or the hand-eye calibration between robot and endoscope. In addition, it is able to achieve the singularity avoidance task and subsequently prevents the robots from being out of control. This advantage is crucial for the safe manipulation

of robots during minimally invasive surgeries since it is less probable to cause harm to the patients. To the best of our knowledge, this is the first work that proposes a singularity-avoidance visual servoing algorithm for continuum tubular robots.

- Cadaveric studies have been implemented to demonstrate the reliability and superiority of the proposed singularity-avoidance visual servoing algorithm.
- Four candidate image processing algorithms are proposed and investigated. Based on the images collected during the cadaveric experiments, an optimal image processing framework within the four candidate algorithms is determined for visual servoing tasks in a surgical environment.

The rest of the paper is organized as follows. Section II introduces the mechanical design of the continuum tubular robot investigated in this paper. Four different image processing frameworks are presented in Section III, including comparison and discussion. Section IV proposes a model-free visual servoing system based on desirable image tracking results. The singularity problem of robotic control is stated and analyzed and singularity-avoidance mechanisms are proposed in Section V. The experiment results are comprehensively reported in Section VI. Section VII gives a summary of the entire paper and includes relevant discussions. Finally, the conclusion is provided in Section VIII.

II. MECHANICAL DESIGN

The mechanical setup of the overall system is shown in Figure 1(a). The robot comprises two concentric tubes (outer and inner), each having a rotational degree-of-freedom (DOF) and a translational DOF, accumulating to 4 DOFs in total. When the outer tube is straight, its rotation does not affect either the position or the orientation of the tip, so the robot degenerates to 3 DOF. The magnified image on the left illustrates the telescopic design of the visual component, wherein a flexible endoscope with small dimensions is mounted at the end-effector of this CTR to provide visual feedback. With image feedback being utilized to guide the robot, the target on the image plane can be moved from the initial position to the desired region. In addition, the eye-in-hand visual servomechanism is illustrated in Figure 1(b), wherein the origin of the base coordinate O_c is located at the back-end of the actuation system, while the origin camera coordinate O_b coincides with the distal tip of the CTR. The image position for the 3D points in the space can be projected onto the image coordinate $[u, v]$.

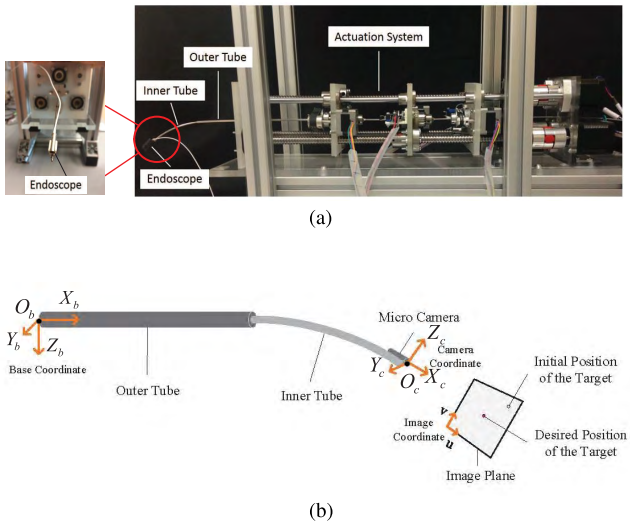

FIGURE 1. The system design of our CTR under study. (a) The overall system consists of a continuum tubular robot and an endoscope attached at the tip of the robot. (b) The eye-in-hand visual servoing setup.

For the proposed CTR, when the curved (outer and inner) tubes are inserted inside each other, their common axis conforms to a mutually resultant curvature. In our design, the ratio of bending stiffness for the two tubes is rather large, such that the shape of the outer tube dominates that of the inner. Since the bending stiffness of one tube is much larger than that of the other, the pair of continuum tubes can conform to the curvature of the stiffer (outer) tube. When the more flexible (inner) tube is translated such that it extends beyond the end of the stiff tube, the extended portion relaxes to its original curvature. Therefore, the snap problem of tubes can be solved through this special mechanical design.

III. IMAGE PROCESSING ALGORITHMS

As introduced above, the objective of visual guidance is to track the surgical target and manipulate the end-effector to the desired position on the image plane, namely an image-based visual servoing (IBVS) problem. In order to achieve proper positioning, the first step is to detect and track the relevant image features from the endoscopic image sequences. In this study, a laser pointer is used to highlight the target surgical sites. Four different image processing approaches have been investigated to extract the laser marker from the images captured by the endoscope.

Since the laser marker is usually brighter than the surroundings, an intensity-based procedure, similar to the procedure introduced in [32] can be adopted to extract the contour of the laser marker. Then, the position of the surgical target can be represented by the centroid of the marker and calculated based on the moment of the contour pixels as expressed below

$$m_{ij} = \sum_{x,y} I(x, y) \cdot x^i \cdot y^j \tag{1}$$

where m_{ij} indicates the raw image moments.

Therefore, the x and y coordinates of the marker centroid can be acquired using

$$\bar{x} = \frac{m_{10}}{m_{00}}, \bar{y} = \frac{m_{01}}{m_{00}} \tag{2}$$

The four image processing techniques will be covered in the following subsections with a comparison of image tracking performances.

A. SALIENCY-BASED METHOD

Salient object detection can be used to improve detection accuracy since the laser marker on the image plane is usually the most salient region. Because of their outstanding performance, two existing saliency estimation methods are selected to be incorporated into the image processing frameworks respectively, including the background detection (BD) assisted method proposed in [37] and the graph-based manifold ranking (MR) approach introduced in [38].

After image preprocessing, the salient regions of the resultant contrast-enhanced image can be extracted based on the aforementioned two saliency detection algorithms. Additional image processing is performed to acquire the contour and successively locate the center coordinate of the laser marker. To this end, the resulting grayscale image first undergoes thresholding based on gray values, and the undesired noises are eliminated by removing tiny regions. The integrity of the marker is guaranteed by filling up the empty spaces between the detected pieces of the marker. Subsequently, Sobel edge detection is implemented to identify the contours in the resultant binary image. The coordinates of the centroid of the marker are then calculated based on Eq. (2).

B. INTENSITY- AND GRADIENT-BASED METHOD

Different from the saliency-based method, image intensity, and gradient can be used as geometrical features to track the region of interest. The rationale of the intensity and gradient-based algorithm is that the intensity of the marker is distinguishable from that of the surrounding tissues, and the image gradient at the contour of the marker is usually the maximum. In this paper, an intensity-based and a combined intensity-gradient-based image processing method are developed and tested in surgical environments. The proposed intensity and gradient-based image processing method can be summarized, as depicted in Figure 2.

With respect to the intensity-based processing, the original RGB image (I) is split into its three channels and the red channel image (R) is extracted since the intensity of the marker is the strongest in this channel. To improve the efficiency of thresholding, a processed image (P) is obtained as the weighted sum of the original image and the red channel image as expressed in $P = \lambda I + \mu R$, where λ and μ represent two constant weight coefficients. The two coefficients are set to 0.6 and 0.4 respectively to achieve the optimal performance according to the experiments.

Regarding the gradient-based processing, the captured image is first converted to a gray-scale image; subsequently, both horizontal and vertical derivatives of each pixel are calculated. The gradient of each pixel is then defined as

$$G_{ij} = \frac{1}{2}G_x^{ij} + \frac{1}{2}G_y^{ij} \tag{3}$$

where G_{ij} represents the intensity gradient of pixel at (i, j) while G_x^{ij} and G_y^{ij} indicate the x and y derivatives of this pixel, respectively. Thresholding is then implemented on the resultant gradient image to enhance the gradient variance. That is, if the intensity of a pixel in the gradient image is lower than the threshold, which is set as 40 in our case, then the pixel intensity will be reset to 0. Otherwise, the pixel intensity is updated to 255.

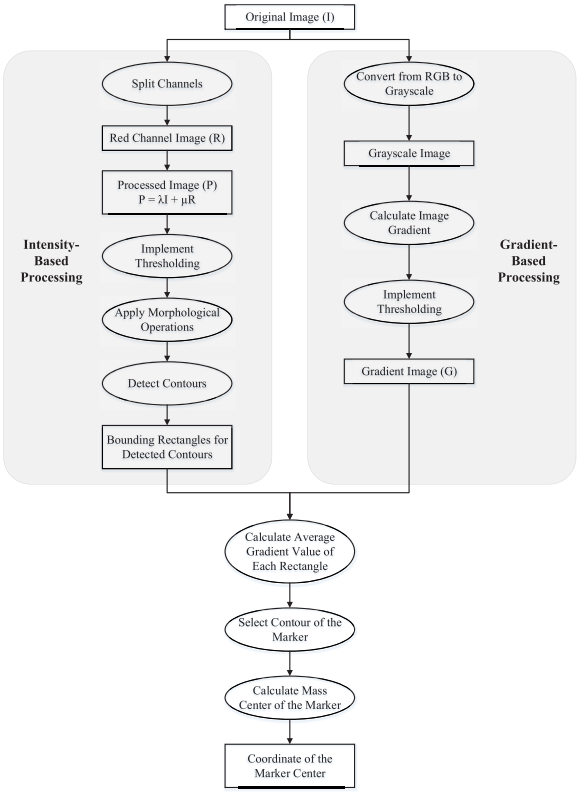

FIGURE 2. Framework of the intensity- and gradient-based image processing approach.

A binary image is then obtained via implementation of thresholding on the processed image to screen out pixels with lower intensity. Morphological operations are then carried out to eliminate the noises and ensure the completeness of the detected marker. Following all contours are detected using canny edge detection, a bounding rectangle for each contour is calculated. Regarding each rectangle, the gradient value of each pixel inside is obtained by checking the gradient image. The average gradient value of the bounding rectangle is then defined as the sum of the gradient values of all pixels inside the rectangle, divided by the total number of pixels within the rectangle. The contour of the marker can then be selected from all the detected contours based on the average gradient value. That is, the contour which is bounded by the rectangle with the largest average gradient value is recognized as the contour of the marker since the significant distinction between the marker and the surrounding tissues makes the gradient variation at this area most noticeable. The position of the marker center can subsequently be determined according to Eq. (2).

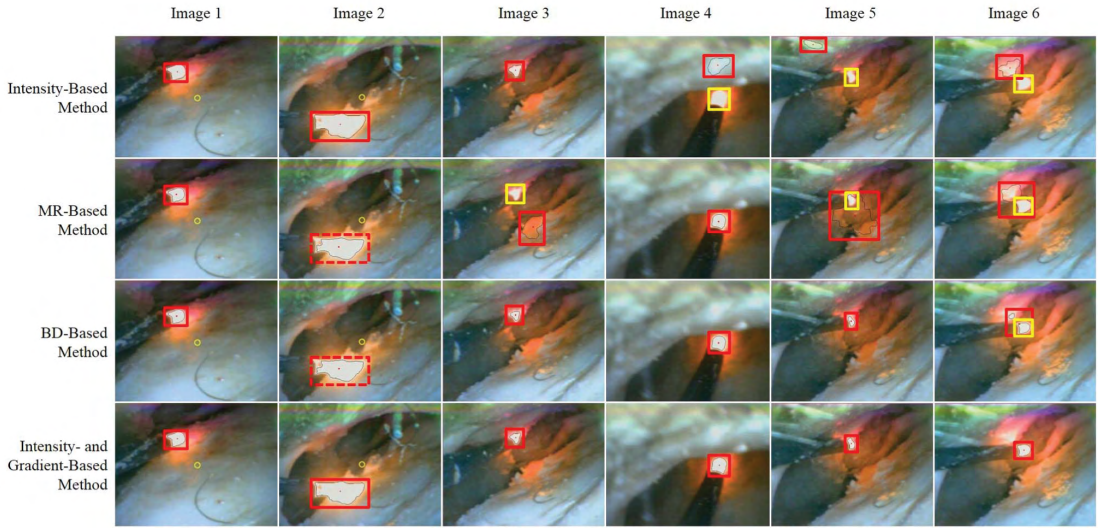

FIGURE 3. The highlighted surgical targets on six sample figures using different image processing algorithms. The black curves and red dots represent the contours and centroids of the targets, respectively. The red and yellow rectangles indicate the detected and actual locations of the targets, respectively. The red dotted rectangles demonstrate the less accurate, although acceptable detection results.

C. PERFORMANCE COMPARISON USING DIFFERENT METHODS

To evaluate and compare the four image processing approaches, offline images of the tissues with target surgical sites highlighted using the laser markers were collected during the cadaveric experiments, and the algorithms were implemented to extract the center position of the marker on the image plane. In total, 10010 valid pictures were collected, and for each picture, all four algorithms were applied to detect the marker location. The detection was recorded as successful if the location of the marker was correctly identified; otherwise, it was regarded as failed. The success rates and time overhead to process each image frame of the image processing techniques are listed in Table 1. It can be concluded that adopting the proposed intensity- and gradient-based method leads to the best detection results, given that the additional time consumption is acceptable.

TABLE 1. Success rates of the image processing methods.

Methods	Success Rate	Time consumption
Intensity-Based Method	94.63%	0.018 s/frame
MR-Based Method	92.81%	0.017 s/frame
BD-Based Method	96.06%	0.020 s/frame
Intensity- and Gradient-Based Method	99.61%	0.022 s/frame

To present these findings in a more intuitive way, six different sample pictures captured from different sites are selected to investigate the four algorithms as depicted in Figure 3. In this figure, the contours of the surgical targets are marked with black curves, while the centroids of the targets are highlighted using red dots. The red rectangles frame the detected contours while the yellow rectangles frame the actual contours. If the detected contour overlaps the actual contour, only a red rectangle is displayed. A red dotted rectangle represents a less accurate, although acceptable detection result. Because of the outstanding performance of the intensity- and gradient-based processing method, it was adopted to extract the positions of the targets in the following visual servomechanism.

IV. MODEL-FREE VISUAL SERVOING

Compared to eye-to-hand visual servoing which requires more working space, eye-in-hand visual servoing is more practical during surgery. Further, since model-based methods are generally complicated and no longer accurate in limited working environments, a model-free approach is more promising in practical applications. Therefore, we have proposed a model-free eye-in-hand visual servoing (MFVS) framework for a continuum tubular robot as shown in Figure 4.

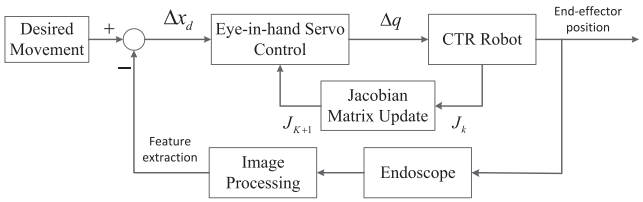

FIGURE 4. Control diagram of the model-free eye-in-hand visual servomechanism.

Based on the coordinate difference between the target position and current position of the marker center, the desired translation of the marker on the image plane can be determined as

$$\Delta x_d = x_n - x_k \tag{4}$$

where Δx_d represents the desired displacement of the marker, x_k indicates the current position of the marker, and x_n is the next reference position to reach. The next reference position to reach on the image plane is defined as

$$u_r = \begin{cases} u_m + \dfrac{\eta(u_t - u_m)}{\sqrt{(u_t - u_m)^2 + (v_t - v_m)^2}} \\ \sqrt{(u_t - u_m)^2 + (v_t - v_m)^2} > \eta \\ u_t \quad otherwise \end{cases}$$

$$v_r = \begin{cases} v_m + \dfrac{\eta(v_t - v_m)}{\sqrt{(u_t - u_m)^2 + (v_t - v_m)^2}} \\ \sqrt{(u_t - u_m)^2 + (v_t - v_m)^2} > \eta \\ v_t \quad otherwise \end{cases} \tag{5}$$

where (u_t, v_t), (u_m, v_m) and (u_r, v_r) represent the center of the target region, the current position of the marker, and the next reference coordinate for the marker to reach, respectively. In addition, η serves as a gain parameter, indicating the step size of the marker movement on the image plane and scaling the difference between the target center and the current position of the marker. A suitable value of $\eta = 10$ was carefully tuned by experimentation to provide an effective visual servoing. Based on the desired movement of the marker, the actuators are controlled accordingly using

$$\Delta q_k = J_k^{\dagger} \Delta x_d \tag{6}$$

where $J_k^{\dagger}$ indicates the pseudo-inverse of the Jacobian matrix. The Jacobian matrix relates the actuator movements in the joint space with the position change of the target on the image plane.

To update the Jacobian matrix online, the basic framework mainly consists of the following steps, starting with Jacobian initialization [33]. Since no prior knowledge of the kinematic model is provided, the Jacobian can only be roughly estimated by establishing the relationship between movements of the actuators and coordinate change of the marker on the image plane. To this end, each individual actuator is run separately and the coordinate change of the marker is determined at the same time. Then, the initial Jacobian matrix is estimated using

$$J = \begin{bmatrix} \dfrac{\partial f(q)}{\partial q_1} & \dfrac{\partial f(q)}{\partial q_2} & \dfrac{\partial f(q)}{\partial q_3} \end{bmatrix} \tag{7}$$

where $f(q)$ is the 2D coordinate of the marker, and q_i indicates the $i-th$ joint input. More specifically, q_1 is the simultaneous translation of the outer and inner tubes. The q_2 and q_3 are the translation and rotation of the inner tube, respectively.

After the movement is completed, the actual displacement of the marker is measured and denoted as Δx_k. The updated Jacobian matrix can subsequently be obtained by solving

$$min\ ||\Delta J_k||_F \quad s.t.\ \Delta x_k = (J_k + \Delta J_k)\Delta q_k. \tag{8}$$

By adopting the Frobenius norm, a closed form solution to this problem can be acquired. Let

$$b = \Delta x_k - J_k \Delta q_k \in \mathbb{R}^{2\times 1} \tag{9}$$

$$A = \begin{pmatrix} \Delta q_k^T & 0 \\ 0 & \Delta q_k^T \end{pmatrix} \in \mathbb{R}^{2\times 2r} \tag{10}$$

and re-organize

$$\Delta J_k = \begin{bmatrix} \Delta J_{k,1}^T \\ \Delta J_{k,2}^T \end{bmatrix} \in \mathbb{R}^{2\times r} \tag{11}$$

to

$$\Delta j_k = \begin{bmatrix} \Delta J_{k,1} \\ \Delta J_{k,2} \end{bmatrix} \in \mathbb{R}^{2r\times 1}, \tag{12}$$

Eq. (8) can be rewritten as

$$A\Delta j_k = b. \tag{13}$$

Since the solution to minimizing $||\Delta j_k||_F$ is

$$\Delta j_k = A^T(AA^T)^{-1}b, \tag{14}$$

and

$$||\Delta J_k||_F = ||\Delta j_k||_F, \tag{15}$$

ΔJ_k can be solved by rewriting

$$\Delta j_k = \begin{bmatrix} \Delta q_k(\Delta q_k^T \Delta q_k)^{-1} b_1 \\ \Delta q_k(\Delta q_k^T \Delta q_k)^{-1} b_2 \end{bmatrix} \tag{16}$$

to

$$\Delta J_k = \begin{bmatrix} b_1(\Delta q_k^T \Delta q_k)^{-1}\Delta q_k^T \\ b_2(\Delta q_k^T \Delta q_k)^{-1}\Delta q_k^T \end{bmatrix}. \tag{17}$$

Therefore, the updated Jacobian can be expressed as

$$J_{k+1} = J_k + \kappa \frac{(\Delta x_k - J_k \Delta q_k)\Delta q_k^T}{\Delta q_k^T \Delta q_k} \tag{18}$$

where J_{k+1} and J_k are the updated and previously estimated Jacobian, respectively, while κ is an update rate to avoid overshoot. In the MFVS algorithm, κ is simply set to a constant.

Furthermore, the stability analysis is discussed in the Appendix.

V. SINGULARITY PROBLEM: ANALYSIS AND AVOIDANCE

A. PROBLEM DESCRIPTION

Generally, the control of the robot and the update of the Jacobian is iteratively implemented until the marker is moved into the desired region. However, the non-redundant robot can encounter singularity problems in practical applications. For example, internal singularities can cause excessive joint speed requirements that cannot be realized by the actuators, thus causing errors in a specified trajectory. In order to overcome the shortcomings inherent in non-redundant robots, redundant robots have been utilized to increase flexibility and dexterity around a restricted task space in the presence of obstacles [39].

Given a visual servomechanism, the image Jacobian matrix J_k, or its pseudo-inverse matrix $J_k^{\dagger}$, become singular during the servoing process, leading to an unstable behavior in the closed loop. It is well known that the image Jacobian is singular if the feature point matrix is composed by the

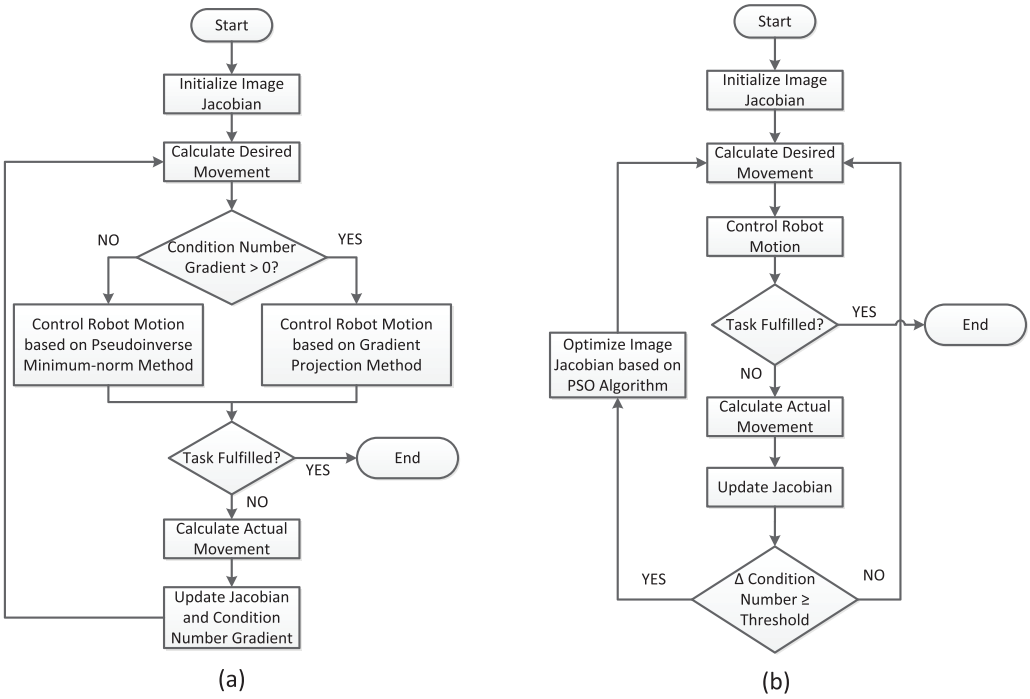

FIGURE 5. Flowcharts of the two proposed visual servoing algorithms: (a) illustrates the framework of SRVS-GP, (b) illustrates the framework of SRVS-JO.

three feature points such that they are collinear, or belong to a cylinder containing the camera optical center [40].

Condition number, which is defined as the ratio of the largest to the smallest singular values of a matrix, commonly provides a good measure of ill-conditioning of the matrix [41]. Generally, when the Jacobian matrix reaches the singularity, its condition number becomes infinite [42]. Therefore, the condition number can be regarded as a parameter to be carefully tuned during the visual servoing process, in order to overcome the effect of Jacobian singularity. The following two subsections will discuss two possible solutions to deal with the problem of Jacobian singularity with the help of condition number.

B. SINGULARITY AVOIDANCE BASED ON GRADIENT PROJECTION

First, based on the singularity avoidance method proposed in [36], a singularity-avoidance visual servoing approach based on Gradient Projection technique (SRVS-GP) can be derived by modifying the above model-free visual servoing framework. Since the developed eye-in-hand robotic system is redundant, the Gradient Projection (GP) method can be adopted instead of the pseudo-inverse minimum-norm method when solving for the actuator motion [43]. The overall framework of the SRVS-GP algorithm is shown in Figure 5(a).

As mentioned above, since the condition number can be regarded as a valid measure of Jacobian singularity, minimizing the condition number of the Jacobian matrix can be a secondary task during the visual servoing process. The movement of the actuators can then be calculated according to

$$\Delta q_k = J_k^{\dagger} \Delta x_d - \gamma (I - J_k^{\dagger} J_k) \dot{h}_k \tag{19}$$

where I is the identity matrix and h_k indicates the condition number of J_k, which is defined as the ratio of its largest singular value $\sigma_{max}(J_k)$ to its smallest singular value $\sigma_{min}(J_k)$ as shown in

$$h_k = \frac{\sigma_{max}(J_k)}{\sigma_{min}(J_k)}. \tag{20}$$

Thus, $\dot{h}_k$ is a vector with the same dimension as the joint space. In addition, the weight coefficient of the secondary task is denoted as γ to tune the impact of the additional task so that no overshoot in the end-effector is caused due to the large value of γ, while sufficient effort is made to avoid the singularity of the Jacobian.

In this way, the components of the gradient of h_k are selected in the null space of the Jacobian J by the projection operator $(I - J_k^{\dagger} J_k)$ so that the condition number of the Jacobian is minimized, while the performance of the image based position control is not affected. Meanwhile, the gradient of the condition number in the secondary task can be estimated from several linearly independent motions, based on the Broyden's updating formula in

$$\dot{h}_{k+1} = \dot{h}_k + \frac{(\Delta cond_k - \dot{h}_k \Delta q_k) \Delta q_k^T}{\Delta q_k^T \Delta q_k} \tag{21}$$

where $\Delta cond_k$ indicates the condition number change between time k and $k-1$. Δq_k represents the actuated

movement of each joint. $\dot{h}_{k+1}$ and $\dot{h}_k$ are the updated gradient of condition number at time $k+1$, and the previously estimated gradient at time k, respectively.

However, since the ultimate goal is to avoid singularity rather than to have Jacobian with a low condition number, the motion of the continuum tubular robot is controlled using the GP method when the gradient of the condition number is positive. Otherwise, the motion is controlled based on the pseudo-inverse minimum-norm method.

C. SINGULARITY-RESISTANT JACOBIAN OPTIMIZATION

Although the SRVS-GP approach is likely to solve the Jacobian singularity problem, its influence on the performance of visual servoing is usually difficult to regulate. Therefore, instead of modifying the motion control method, a more reliable singularity-resistant visual servoing method based on Jacobian Optimization (SRVS-JO) during the Jacobian update process is proposed to better address the singularity avoidance challenge. The flowchart of the proposed SRVS-JO method is presented in Figure 5(b). The optimization of the estimated Jacobian is achieved by tuning the update rate in Eq. (18), rather than adopting it as a constant value so that the Jacobian singularity is avoided while updating the Jacobian matrix based on actual movements of the marker on the image plane.

Optimization of the Jacobian matrix is achieved by adopting the Particle Swarm Optimization (PSO) algorithm because of its robustness and high computational efficiency. The PSO technique is a population-based, stochastic optimization algorithm inspired by the social behavior of flocking birds or schooling fish [44]. The mechanism is used to search for an appropriate value for the update rate κ so that the property of the Jacobian matrix can be optimized.

Fifty random particle positions representing the candidate values of the update rate are initially created, with each of them being denoted as K_i. Moreover, fifty randomly generated velocities V_i are assigned to these particles correspondingly. Based on the objective function, each particle location is then evaluated to determine the best function value and its corresponding location. Then the velocities and locations of the particles are iteratively updated. The new velocities V_i^{t+1} are updated based on the current velocities V_i^t, each individual particle's optimal results P_i^t, and the present global optimal result P_g^t as indicated in

$$V_i^{t+1} = \omega V_i^t + c_1 R_1 (P_i^t - K_i^t) + c_2 R_2 (P_g^t - K_i^t) \quad (22)$$

where ω indicates the inertia weight, c_1, c_2 are two constant acceleration factors, and R_1, R_2 represent two random factors in the [0, 1] interval. The constants c1 and c2 represent the weighting of the stochastic acceleration terms that pull each particle toward the optimal positions. Low values allow particles to roam far from the target regions before being tugged back. On the other hand, high values result in an abrupt movement toward or past target regions. According to [45], the inertia weight and two constant acceleration factors are set to 0.8, 2 and 2, respectively.

Based on the updated velocities, the particle positions are subsequently updated using

$$K_i^{t+1} = K_i^t + V_i^{t+1} \quad (23)$$

where K_i^{t+1} and K_i^t are the updated position and previous position of each particle, respectively.

The iteration terminates when the specified maximum iteration number is reached or the changes in global optimal results from multiple iterations are minor. The maximum number of iterations is set to 50 for the clinical trials. During the experiments, the average iteration number is 23, with a minimum value of 8 and a maximum value of 39.

As previously mentioned, the objective of the algorithm is to avoid singularity of the Jacobian instead of acquiring the Jacobian with the lowest condition number. Therefore, an additional condition is to be satisfied before implementing the Jacobian Optimization procedure. In the proposed algorithm, the variation in the condition numbers between two adjacently estimated Jacobian matrices is assessed. Only if the increment exceeds a specific threshold will the optimization process be executed.

In addition, the SRVS-JO algorithm can be divided into two types based on the objective functions adopted during the process of PSO. First, the condition number of the updated Jacobian can be regarded as an object to be minimized, as expressed in

$$\begin{aligned} &\underset{\kappa}{\text{minimize}} \ \frac{\sigma_{max}(J_k)}{\sigma_{min}(J_k)} \\ &\text{subject to } J_{k+1} = J_k + \kappa \frac{(\Delta x_k - J_k \Delta q_k)\Delta q_k^T}{\Delta q_k^T \Delta q_k} \end{aligned} \quad (24)$$

where $\sigma_{max}(J_k)$ is the largest singular value of the Jacobian matrix, and $\sigma_{min}(J_k)$ is the smallest singular value.

Another possible objective function for optimization is the absolute change between the condition numbers of two consecutively estimated Jacobian matrices. The update rate can be obtained through

$$\begin{aligned} &\underset{\kappa}{\text{minimize}} \ \left| \frac{\sigma_{max}(J_{k+1})}{\sigma_{min}(J_{k+1})} - \frac{\sigma_{max}(J_k)}{\sigma_{min}(J_k)} \right| \\ &\text{subject to } J_{k+1} = J_k + \kappa \frac{(\Delta x_k - J_k \Delta q_k)\Delta q_k^T}{\Delta q_k^T \Delta q_k} \end{aligned} \quad (25)$$

where $\sigma_{max}(J_{k+1})$ and $\sigma_{min}(J_{k+1})$ are the largest and smallest singular values of the updated Jacobian J_{k+1}, respectively. The rationale behind this objective function is that the initialized Jacobian matrix is usually in good condition while the ill-condition happens during the subsequent estimation process in the confined environment. Therefore, the singularity can be avoided by assuring that the change in condition numbers between adjacently estimated Jacobians is limited.

To differentiate the two Jacobian Optimization based visual servoing methods, the algorithm that adopts the condition number as the objective function is referred to as SRVS-JO-CN in the following section of the paper, while the method utilizing the absolute condition number difference as the objective function is referred to as SRVS-JO-CND.

VI. EXPERIMENT RESULTS

A. SIMULATION RESULTS

To demonstrate and compare the performance of the model-free eye-in-hand visual servoing algorithms, simulation experiments were first carried out with the setup shown in Figure 1(b). The simulation follows the actual visual servoing procedure introduced in Section III and IV. The parameter settings are listed in Table 2. In addition, different degrees of noises were added when detecting the target position during the visual servoing process to mimic the unexpected situations in confined environments. There were four different levels of noise added in total with the lowest noise being set to $e_u, e_v \sim \mathcal{U}(-5, 5)/pixel$, and the highest noise being set to $e_u, e_v \sim \mathcal{U}(-20, 20)/pixel$, where $\mathcal{U}()$ represented uniform distribution.

TABLE 2. Parameters for simulation.

Parameters	Values
Camera Resolution	$720*625\ pixels^2$
Target Marker Position (Image Coordinate)	$(320, 240)/pixel$
Initial Marker Position (Base Coordinate)	$(80, 20, 150)/mm$
Camera Intrinsic Matrix	$\begin{bmatrix} 682.7 & 0 & 320 \\ 0 & 682.7 & 240 \\ 0 & 0 & 1 \end{bmatrix}$
Outer Tube Curvature	$0/mm^{-1}$
Inner Tube Curvature	$0.0125/mm^{-1}$
Initial Robot Joint Variables	$s_1 = 50mm, s_2 = 50mm, \theta_2 = 0rad$

Since the noises were randomly generated, the simulation with each noise level was executed 100 times for each algorithm. The mean values and standard deviations of the pixel distances between the actual and reference trajectories resulting from implementing each algorithm are calculated and presented in Figure 6. The mean values, as well as the standard deviations of the average condition numbers of the Jacobian matrices when implementing each visual servoing algorithm are demonstrated in Figure 7.

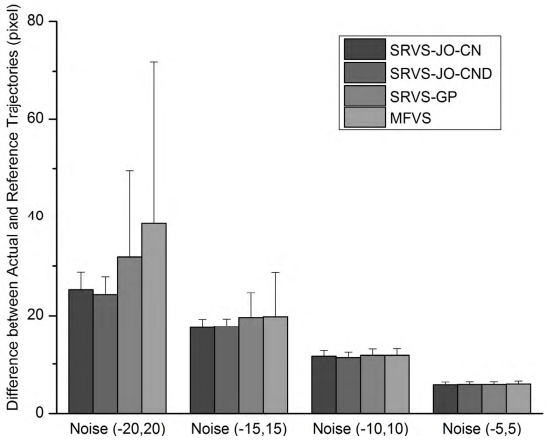

FIGURE 6. Mean values and standard deviations of the average pixel distance between the actual and reference trajectories after implementing each visual servoing algorithm under each level of noise for 100 times.

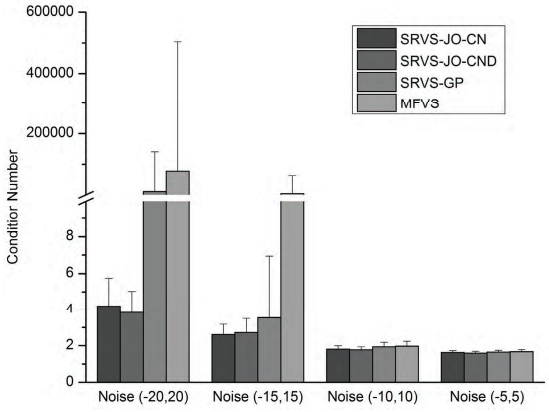

FIGURE 7. Mean values and standard deviations of the average condition number of the Jacobian matrices after implementing each visual servoing algorithm under each level of noise for 100 times.

As revealed in the two figures, the efficiency of the visual servoing techniques was affected by the introduction of noise. That is, the performance of all the investigated algorithms became worse with increasing noise. More importantly, the superiority of the proposed SRVS-JO methods, including both the SRVS-JO-CN and SRVS-JO-CND algorithms, was obvious when compared with the other two algorithms. The superiority previously mentioned was especially apparent when evaluating the condition number of the Jacobian. Compared with average pixel distance between actual and reference trajectories, average condition number is considered a better criterion for assessing the algorithms. The reason is that more strictly following the reference trajectory is likely to lead to a less optimal performance in confined environments, which results in a more complicated path and in turn requires more steps. However, the condition number of the Jacobian matrix is sensitive to singularity situations and thus a smaller average condition number usually indicates a more singularity-robust path.

B. CHALLENGING TASKS WITH SINGULARITY AVOIDANCE

To evaluate the image-guided CTR with the singularity avoidance for target reaching, we are investigating representative tasks involving singularity avoidance as follows. When the Jacobian matrix is not full-rank, the robotic system is said to be in a singular configuration. Mathematically, the overall visual-motor Jacobian from the image space to the actual space, $J_I(q)$, can be further decomposed to $J_I(e)$, the image Jacobian matrix mapping from end-effector or endoscope space to Image space, and $J_e(q)$, the manipulator Jacobian matrix mapping from actuator space to end-effector or endoscope space in Cartesian format, as given by,

$$J_I(q) = J_I(e) * J_e(q). \tag{26}$$

According to the theorem for the rank of the product of two matrices, the overall Jacobian singular configuration, $J_I(q)$, can be determined by its decomposed Jacobian matrices,

$$rank(J_I(q)) \leq \min(rank(J_I(e)), rank(J_e(q))). \quad (27)$$

Therefore, when either $J_I(e)$ or $J_e(q)$ loses rank, the rank of overall $J_I(q)$ reduces accordingly. Utilizing this property, we can identify representative singular configurations from the rank-deficient cases of either the image Jacobian matrix ($J_I(e)$) or manipulator Jacobian matrix ($J_e(q)$).

In confined surgical environments, the CTR singularity configurations appear when: 1) the position of the target on the image plane does not vary with the movement of at least one actuator or 2) the movements of at least two different actuators result in similar position change of the target in the image coordinate. Specifically, we discuss the following representative singular configurations.

1) SINGULAR CONFIGURATION 1

When the inner tube is hidden inside the outer tube, the entire robot configuration is a straight line with only translational motion, which forms a singular configuration in the manipulator Jacobian, i.e., $J_e(q)$ has a rank loss. If simultaneously the image feature points are co-linear with the optical axis, this will form a singular configuration in the image Jacobian matrix ($J_I(e)$). When the robot starts moving, this configuration is easy to escape by extending the inner tube from the outer tube. Because of the elastic tube pre-curvature, the inner tube will restore to the load-free mode and thus get away from the singular configuration.

2) SINGULAR CONFIGURATION 2

A manipulator Jacobian, $J_e(q)$, is rank-deficient when the simultaneous translation of the outer and inner tubes and the translation of the inner tube cause the same tip motion. This robotic singular configuration can be avoided by imposing an additional constraint to the relative motion between the outer and inner tubes, which has been discussed in our earlier publication [32]. Due to the unique tubular motion generation mechanism of a CTR by translating a pre-curved elastic tube, this singular configuration is especially existing in the concentric tube robot mechanism and is unlikely seen in articulated rigid-body industrial arms nor in cable-driven flexible manipulators [4]. Well-defined relative translations of one outer tube and one inner tube can result-in 2-DOF end-effector motion in Cartesian space, which has a full-rank motor-manipulator Jacobian matrix.

3) SINGULAR CONFIGURATION 3

$J_I(e)$ is not full-rank if the feature point matrix is composed by the image feature points such that they are collinear, or belong to a cylinder containing the camera optical center [36]. Following the Section VI-A, we use the similar simulation setup to evaluate the algorithm effectiveness of singularity avoidance using the MFVS and SRVS-JO-CN algorithms, as shown in Figure 8 and Figure 9. The target

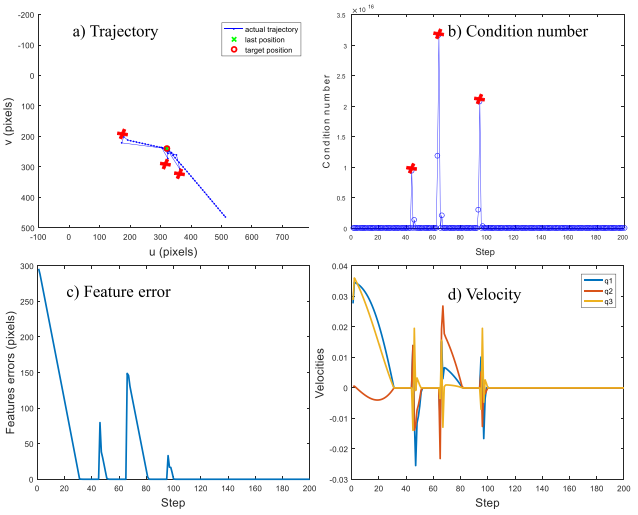

FIGURE 8. The sample image-space trajectory and corresponding condition number, feature error, and motor velocity of the MFVS in Singular configuration 3. A red cross in the figure indicates the event of the abrupt changes following its closeness to the singular configuration, which is corresponding to a local peak condition number. (a): The image-space trajectory. (b): The corresponding condition numbers versus time steps. (c): Feature error. (d): motor velocity in rad per step.

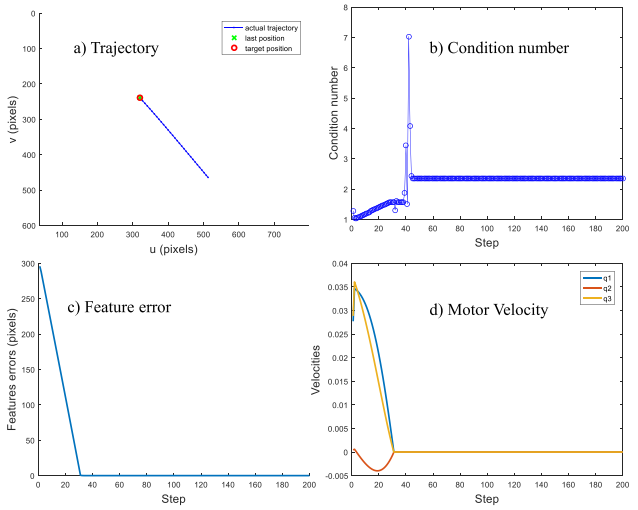

FIGURE 9. The sample image-space trajectory (a) and corresponding condition numbers (b), feature error (c), and motor velocity in rad per step (d) of the SRVS-JO-CN in Singular configuration 3.

maker position is (320, 240) in the image coordinate, which corresponds to the principal point in configuration. The target image-space trajectory is configured to be a straight line at the principal point. In such a configuration, the task corresponds to a pure backward translational endoscope motion along the optical axis, which moves the camera/endoscope at infinity and leads to a singularity.

Using MFVS, the image-plane trajectory shows a high level of instability toward the target point (principal point) due to the singularity of the image Jacobian. The condition number of the corresponding image Jacobian has several sudden changes, as well as the feature error and the velocity.

As indicated by the red crosses in the Figure 8, they show quite abrupt changes in all four subfigures following the attempts to converge to the singular configurations (jumps in condition numbers as well), with the increase/decrease slope nearly infinity. The biggest condition number is up to 3.16×10^{16}. The deteriorated changes in feature error are close to 150 pixels. The direction of the velocity is oscillating, accompanied by abrupt changes in the amplitude between two adjacent steps. The peak condition numbers in subfigure (b) appear a few steps before the abrupt changes in the feature plot (c) and velocity plot (d), which indicate the consequences of incapability of singularity-avoidance. Using SRVS-JO-CN, the optimization algorithm has a better inhibitory effect on the condition number toward the singularity position. It shows much smoother changes, with higher trajectory quality, smaller condition number and convergence steps. The condition number is less than 8 due to the constraint of the Jacobian Optimization algorithm and effectiveness of singularity avoidance. There are little changes in feature error and velocity when converged to the target position. Compared to MFVS, the SRVS-JO-CN algorithm has a better singularity-avoidance performance, exhibiting smaller condition numbers and higher trajectory quality.

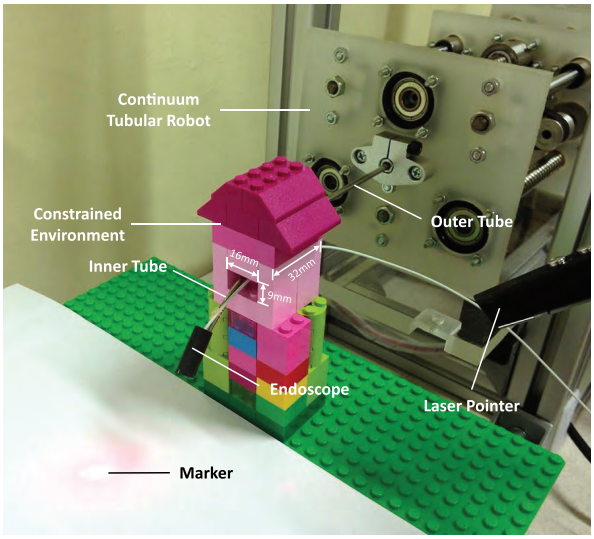

FIGURE 11. The setup of the eye-in-hand system in a confined environment. The internal unseen channel with respect to the Continuum Tubular Robot (CTR) is labeled with dimensions (L: length = 32 mm, W: width=16 mm, H: height=9 mm). The outer and inner diameters of the outer tube are 3.00 mm and 2.20 mm respectively while those of the inner tube are 2.30 mm and 1.75 mm respectively.

4) SINGULAR CONFIGURATION 4

$J_e(q)$ is rank-deficient when the robot is stuck due to its contact with obstacles or its mechanical backlash, resulting in no motion generation at the tip of the robot, despite the movement of actuators.

Like the instantaneous motions described by an ellipsoid in Cartesian space, we can further characterize how close it is to a Jacobian singularity using an ellipsoid with its long axis of the largest singular value, $\sigma_{max}(J_k)$, and short axis of the smallest singular value, $\sigma_{min}(J_k)$. Hence, the shapes of the Jacobian ellipses (named Manipulability Ellipsoid in robotic kinematics) are closely associated with the condition number, which is the ratio of the largest singular value ($\sigma_{max}(J_k)$) and the smallest singular value ($\sigma_{min}(J_k)$). As shown in Figure 10, the red arrow of the long axis indicates more freedom to move (can move a lot) in that specific direction, and the blue arrow of the short axis corresponds to less movable direction.

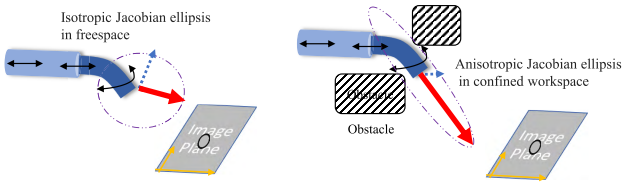

FIGURE 10. The instantaneous CTR visual-motor Jacobian can be described by Jacobian ellipses in the free space (left) and confined space (right). (a) Left sub-figure: The manipulator Jacobian ($J_e(q)$) is nonsingular in the free-space ellipsoid. (b) Right sub-figure: The robot end-effector can be stuck with the obstacles and result in the situation that the robot is experiencing a singularity represented by the anisotropic ellipsis since the motor actuation cannot produce effective visual feature changes.

In the confined space, the robot end-effector can be hindered with the obstacles which can result in the situation where the robot is experiencing a singularity, as shown in the confined-space ellipsoid of Figure 10(b). In this case, the motor actuation cannot produce effective visual feature changes, even though the manipulator Jacobian ($J_e(q)$) is nonsingular in the free-space ellipsoid as shown in Figure 10(a). Therefore, it is critical to prevent the overall system Jacobian from being further trapped into even more singular space (meaning larger condition number). This prevention is closely associated with the process of updating and optimizing overall Jacobian iterations.

Generally, we have focused on the singularity avoidance in confined clinical environments using a model-free data-driven visual servoing approach based on Jacobian estimation. Modeling obstacles as constraints can be a separate model-based motion planning problem and complementary to our model-free approach (the focus of this paper). Our earlier publication [46] provided an approximate model of Jacobian matrix and kinematics. However, the model of a continuum tubular robot is generally very complicated and will be distorted when robot-tissue interaction happens in a constrained environment. Therefore as a subsequent study, this paper focuses on a model-free visual servoing approach based on Jacobian estimation to control the motion of a continuum tubular robot.

The next sections will experimentally focus on the last scenario (Singular configuration 4) in confined mock-up environments.

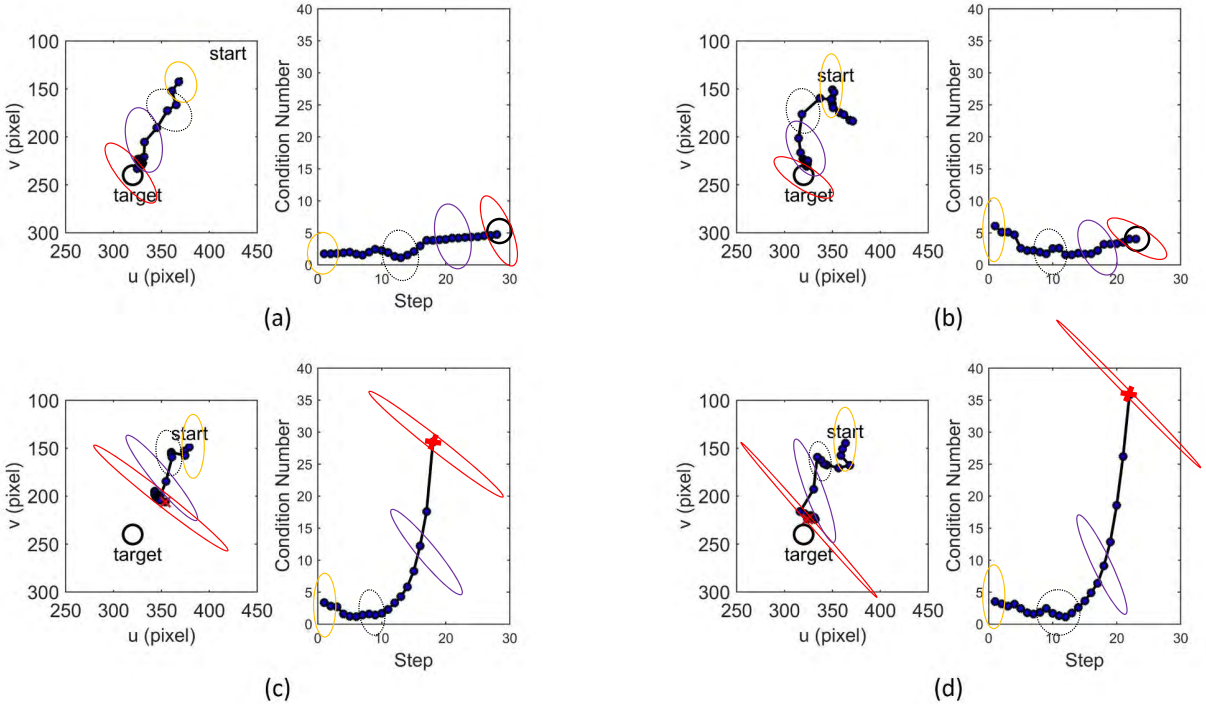

FIGURE 12. The sample trajectory from implementing each visual servoing algorithm in the confined environment is on the left. On the right shows the corresponding condition numbers and representative Jacobian ellipses of the estimated Jacobian matrices along the time steps. The orange ellipses indicate the starting positions, and the red crosses specify the steps when the robot is halted due to its control failure close to the singular configurations. The shapes of the Jacobian ellipses indicate the closeness to the singular configurations while getting more anisotropic. (a) The trajectory and the condition number chart when adopting the SRVS-JO-CN algorithm. (b) The trajectory and condition number chart when adopting the SRVS-JO-CND algorithm. (c) The trajectory and the condition number chart when adopting the SRVS-GP algorithm. (d) The trajectory and condition number chart when adopting the MFVS algorithm.

C. SINGULARITY AVOIDANCE IN CONFINED MOCK-UP ENVIRONMENTS

More comprehensive singularity-avoidance assessments of the visual servoing techniques were further implemented using the 3 DOF continuum tubular robotic system introduced in Figure 1. The outer and inner diameters of the outer tube were 3.00 mm and 2.20 mm, respectively, while those of the inner tube were 2.30 mm and 1.75 mm, respectively. The endoscope attached at the tip of the robot was 4 mm in diameter. A confined environment was constructed using LEGO bricks as depicted in Figure 11 to mimic the confined space inside the body cavities. A laser pointer was used to generate a marker which specifies the target to be moved to the desired region of the image plane. We evaluate the SRVS-JO-CN, SRVS-JO-CND, SRVS-JO-GP and MFVS algorithms comprehensively in terms of effectiveness of singularity-avoidance (by condition number and Jacobian ellipses), trajectory quality and execution time. The target region coordinates are (240, 320) in image space, as indicated in Figure 12. Each algorithm is executed 8 times to get the statistical measures and totally 32 tests were carried out for evaluating the 4 algorithms.

1) SINGULARITY EVALUATION BY CONDITION NUMBER AND JACOBIAN ELLIPSES

Each visual servoing algorithm was implemented eight times and a sample trajectory on the image plane from implementing each algorithm was demonstrated. The trajectory generated by adopting the SRVS-JO-CN algorithm is shown in Figure 12(a). The trajectory derived from implementing the SRVS-JO-CND algorithm is depicted in Figure 12(b). Similarly, the trajectories from executing the SRVS-GP and the MFVS algorithms are presented in Figure 12(c) and Figure 12(d), respectively. The starting points of the markers were indicated on the image planes and the target regions were circled (black). In addition, the condition number of the estimated Jacobian matrix of each step was listed beside its corresponding trajectory. The representative Jacobian ellipses are re-projected onto the trajectories in the image spaces on the left and onto the plot of condition numbers on the right. The shapes of the Jacobian ellipses indicate the closeness to the singular configurations while getting more anisotropic. In each subfigure, the ellipsoids of the same color and shape in the left-side u-v plot and right-side condition-number plot are indicating the same robot action step.

The target site was moved to the desired location in the image coordinate system after implementing both proposed algorithms (SRVS-JO-CN and SRVS-JO-CND). The task was not completed when the other two methods (SRVS-GP and MFVS) were adopted, and red crosses were used to specify the steps where the motion of the robot was halted as it was too close to a singular configuration and out of control. It can be concluded that the condition number of the Jacobian

dramatically increased when the singularity situation was about to occur, which were indicated by the shapes of the Jacobian ellipses.

As shown in Figure 12 (a)(b), when the proposed SRVS-JO-CN and SRVS-JO-CND algorithms are driving the system within the region of small condition numbers, the Jacobian ellipses are more isotropic in configuration towards a circle, which means a CTR has increasing manipulability in both directions and is farther away from singular configurations. On the contrary in Figure 12 (c)(d), the larger the condition number, the thinner or more anisotropic the ellipsoid is, and the closer to the singular configuration, where the Jacobian determinant is zero and rank-deficient.

For all four visual servoing techniques, the mean values and standard deviations of the average and maximum condition number, from each of the eight trials are stated in Figure 13. The maximum condition number from the MFVS algorithm was 1.71 times higher than that of the SRVS-GP algorithm, and was 9.77 and 10.09 times higher than those of the SRVS-JO-CND and the SRVS-JO-CN algorithms, respectively. In addition, the average condition number of the MFVS algorithm was 1.38, 3.50 and 3.74 times higher than those of the SRVS-GP, the SRVS-JO-CND and the SRVS-JO-CN algorithms, respectively. Therefore, it can be concluded that the two proposed SRVS-JO algorithms significantly outperformed the other two approaches (SRVS-GP and MFVS) in terms of the higher resistance to singular configurations. The SRVS-JO-CN algorithm generated smoother image-space trajectories than the SRVS-JO-CND method, meaning less prone to a local optimum.

TABLE 3. Evaluation summary of implementing the visual servoing algorithms in the confined environment.

	Success Rate	Difference between Actual and Reference Trajectories in Successful Cases (pixels)	Trajectory Quality in Successful Cases
SRVS-JO-CN	100%	10.72±4.83	0.73±0.14
SRVS-JO-CND	100%	17.14±10.68	0.63±0.24
SRVS-GP	25%	18.63±7.27	0.74±0.33
MFVS	12.5%	6.09	0.94

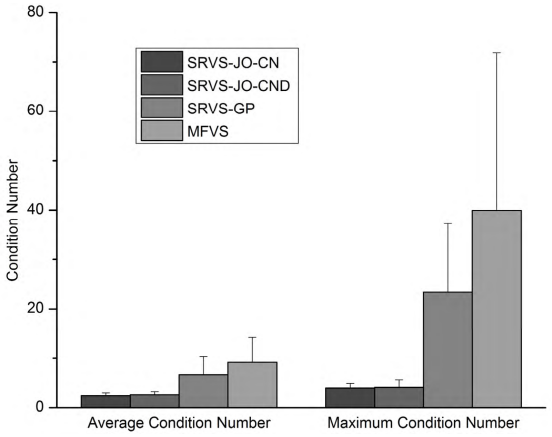

FIGURE 13. Mean values and standard deviations of the average condition number of the Jacobian matrices after implementing each visual servoing algorithm under the confined environment for eight times.

2) TRAJECTORY QUALITY EVALUATION

In addition to condition number and Jacobian ellipses, the quality of the produced trajectory was further evaluated and regarded as another measure of the superiority of the visual servoing methods. Generally, a more direct trajectory is preferred and indicates a more efficient algorithm. Hence, the trajectory quality θ is defined as

$$\theta = \frac{\|x_t - x_i\|}{\sum_{k=1}^{N} \Delta x_k} \tag{28}$$

where Δx_k is the actual movement of the marker in the $k-th$ step, N is the total number of steps required to move the marker to the center of image, while x_t and x_i are the final and initial coordinates of the marker on the image, respectively. Therefore, the trajectory quality ranges between 0 and 1, where a higher value indicates a trajectory with better quality. The evaluation results of the eight sets of experiments are summarized in Table 3, which contains the success rate, average pixel distance between the actual and reference trajectories, and the trajectory quality. Although the trajectory quality was higher when executing the MFVS and SRVS-GP algorithms, the marker was successfully moved to the desired region once when the MFVS method was adopted and twice when the SRVS-GP algorithm was implemented. Therefore, likely the singularity situations were not critical or did not occur during those particular trials. In addition, it can be deduced that the SRVS-JO-CN algorithm outperformed the SRVS-JO-CND algorithm since it led to both smaller condition number and higher trajectory quality.

3) EXECUTION-TIME EVALUATION

The execution times for performing various tasks, including robot control, image processing, and Jacobian update, were calculated separately for all the introduced visual servoing algorithms. The four staked column bars in Figure 14 indicate the average running times for implementing the SRVS-JO-CN, SRVS-JO-CND, SRVS-JO-GP, and MFVS algorithms. The error bars illustrate the slowest and fastest execution times for each method. Based on the charts, it can be concluded that the vast majority of time is spent manipulating the robot (red bars). Due to the introduction of the optimization, it took more time to update the Jacobian when the proposed SRVS-JO algorithms were applied (blue bars), which was anticipated. In addition, the execution times spent on image processing were almost the same between different algorithms (green bars). In general, the overall execution time of different methods can be controlled within $2sec$. Although the SVRS-JO algorithms have a slightly longer execution time than the MFVS approach because of the greater computational burden from Jacobian Optimization.

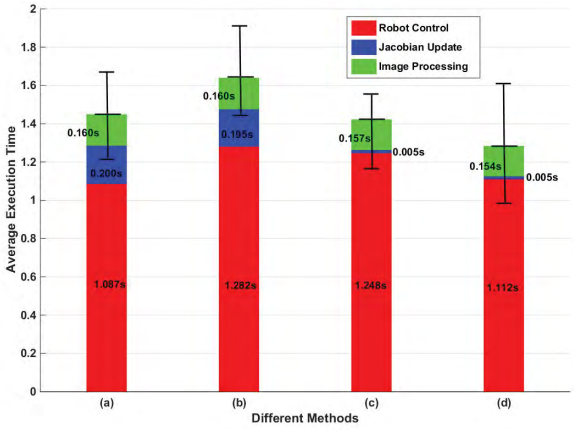

FIGURE 14. Timing charts depicting the execution times to perform various tasks when adopting the four visual servoing methods. (a) Execution times of SRVS-JO-CN. (b) Execution times of SRVS-JO-CND. (c) Execution times of SRVS-GP. (d) Execution times of MFVS.

Considering the minor differences, the superiority in servoing performance leads us to prioritize the proposed methods for real applications.

D. SINGULARITY AVOIDANCE IN CADAVERIC STUDY

Cadaveric studies were further carried out on a human corpse to test the singularity-avoidance effectiveness of the visual servoing algorithms with practical applications. First, a transoral procedure was carried out at the posterior pharyngeal wall as shown in Figure 15. A mouth gag was used to expose the oropharynx, and the entire posterior pharyngeal wall was visualized. In addition, the continuum tubular robot was angled in a more preferable position for the procedure. A pointer was then marked onto the posterior wall at the level of the velopharynx at 3 positions: midline, left paramedian and right paramedian. Different from the previous experiments, an optical fiber, instead of a laser pointer, was used to generate the laser marker and to indicate the target for the robot end-effector, because of its smaller size and flexibility. The lights were projected to the tongue base region including

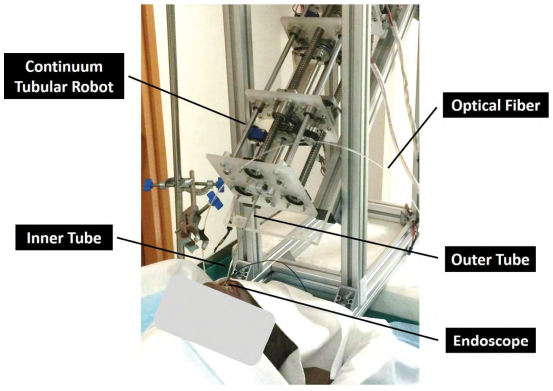

FIGURE 15. Setup for the transoral procedure carried out at the posterior pharyngeal wall.

the epiglottis. It is important to note that reaching that area is challenging and essential for subsequent clinical operations such as a tracheostomy. Targeting control of the continuum tubular robot was performed using the proposed system and the ability of accurately pointing onto the targets was ascertained. A series of 3 consecutive targeting experiments were performed for validity assessment. Figure 16 and Figure 18(a) demonstrate the targeting accuracy and singularity characteristics of targeting the midline of the oropharynx.

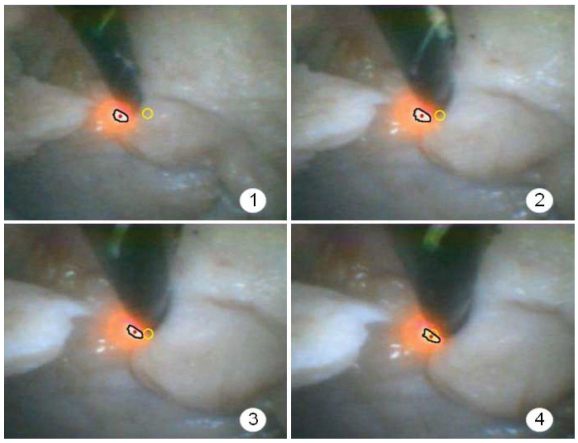

FIGURE 16. Endoscopic image sequence acquired during the transoral visual servoing process in the cadaveric study. Subfigure No.1 shows the initial position of the endoscope, the following subfigures (No.2 and No.3) demonstrate the servoing process until the final state is reached in No.4.

Due to limited access to the cadaver, only the visual servoing algorithms with the best and worst performance were evaluated to emphasize the significance of adopting Jacobian Optimization. These methods were the SRVS-JO-CN algorithm (best singularity-avoidance performance) and the MFVS algorithm (worst singularity-avoidance performance). Each algorithm was executed three times and the designed scenario was to move the desired surgical site which was indicated using the optical fiber to the center of the image plane automatically based on the image feedback.

All three resultant trajectories for each method were shown in Figure 18(a) with the starting position, stop-position, and target region marked on the image plane. In addition, a red cross was used to highlight the point of a task failure where the robot was halted due to its control failure around a singular configuration. Therefore, it can be seen that the singularity-avoidance task was only completed once when the MFVS algorithm was implemented, while it was successfully completed all three times when applying the SRVS-JO-CN method. A sample endoscopic-view visual servoing process applying the SRVS-JO-CN algorithm is shown in Figure 16. The endoscope projection position is indicated by the yellow circle, and the black curve and red dot represent the contour and center of the target surgical site highlighted by the optical fiber, respectively. It can be observed that the end-effector can be manipulated to align to the desired direction in the confined space before moving deeper, as indicated by the

yellow circle intersecting with the black curve. The optical fiber appears in black in Figure 16, since the black tape has been wrapped around the distal end of the optical fiber to gather the light rays.

To quantitatively compare the different visual servoing methods, the average pixel distances between the actual and reference trajectories from executing the SRVS-JO-CN and the MFVS algorithms were 12.64 pixels (approximately 0.93mm) and 15.95 pixels (approximately 1.17mm), respectively. In addition, the trajectory quality arisen from employing the two methods were 0.82 and 0.37, respectively. Therefore, the proposed SRVS-JO technique was superior to the previous visual servoing algorithms in terms of both singularity-avoidance capability and trajectory quality.

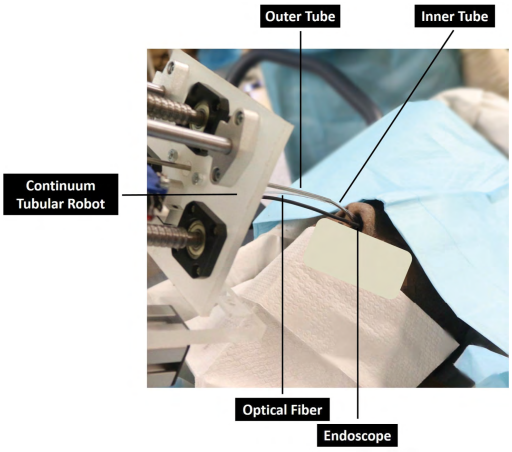

FIGURE 17. Setup for the transnasal procedure carried out at the nasopharynx.

Besides transoral procedures, transnasal procedures were carried out at the nasopharynx, where the workspace of the robot was more constrained. The experiment setup of the visual servoing process conducted inside the nasal cavity is shown in Figure 17. Similar to the transoral procedures, three experiments for each algorithm were carried out. The objective was to move the surgical site highlighted using an optical fiber to the desired region on the image plane while avoiding singular configurations. The main difference between the two procedures is the access routes for pharyngeal surgery, specifically, entering through the patient's mouth for transoral access and the nostril for transnasal access. Transnasal access is subject to stricter environmental constraints than transoral due to narrower canals.

The resultant trajectories are depicted in Figure 18(b). It can be noticed that all three trials failed when the MFVS method was used due to the incapability of avoiding singular configurations, shown as red crosses in the figure. However, all three trials were successful when the SRVS-JO-CN algorithm was implemented. The average pixel distances between the actual and reference trajectories and the trajectory quality were 21.18 pixels (approximately 1.55mm) and 0.44, respectively. The visual servoing process was generally similar to that of the transoral procedure. Based on the experimental results obtained during the transnasal procedures, the superiority of the proposed singularity-avoidance model-free eye-in-hand visual servoing technique was further confirmed.

For both transoral and transnasal procedures, the preparation and setup time is approximately 20 minutes for the first time, and the execution time for each trial of targeting is about 30 to 60 seconds.

VII. DISCUSSION AND LIMITATIONS

This manuscript focuses on motion control of target alignment using continuum tubular robots with image feedback, which is the first important step for a successful robotic nasal-pharyngeal surgery. After successful targeting alignment, other dedicated instruments such as biopsy forceps can be navigated through the lumen of the inner tube for subsequent procedures.

To summarize the methodologies mentioned in this paper, four candidate image processing algorithms, namely intensity-based, MR-based, BD-based and intensity-gradient-based, have been presented and compared in this paper. Based on the images collected during the cadaveric experiments, the proposed intensity-gradient-based framework is identified as the best method and therefore has been adopted during the visual servomechanism. In addition, four eye-in-hand visual servoing algorithms SRVS-JO-CN, SRVS-JO-CND, SRVS-GP, and MGVS have been thoroughly investigated throughout the lab setup and cadaveric experiments. According to the simulation results in Table 3 and the servoing trajectories in Figure 18, the proposed SRVS-JO-CN algorithm is significantly superior to the other 3 methods while performing the visual servoing in confined environments.

In addition, due to the robustness of the proposed singularity-resistant algorithms for confined environments, SRVS-JO-CN and SRVS-JO-CND require no additional restrictions to the singularity problem. The optimal Jacobian matrix, which can be continually updated through the PSO technique, has been proposed to deal with the undefined confined surgical environment. The adaptive tuning processes expressed in Eq. (24) and Eq. (25) elude singularity while updating the image Jacobian matrix based on the actual movement and the computed optimal update rate.

Meanwhile, due to the dedicated applications in surgical confined environments, the following discusses the limitations and corresponding future potential solutions of the CTR with singularity avoidance for target reaching.

A. LIMITATION IN DEPTH PERCEPTION AND POTENTIAL DEPTH-AWARE SOLUTIONS

Monocular endoscopes of small-diameter are widely used in minimally invasive surgeries due to the flexibility and cost-effectiveness. However, with a monocular camera in such a confined working environment where space is limited for additional cameras or depth sensors, it is impractical to build an accurate 3D depth model of the patient's pharyngeal. Two possible solutions can be proposed to address

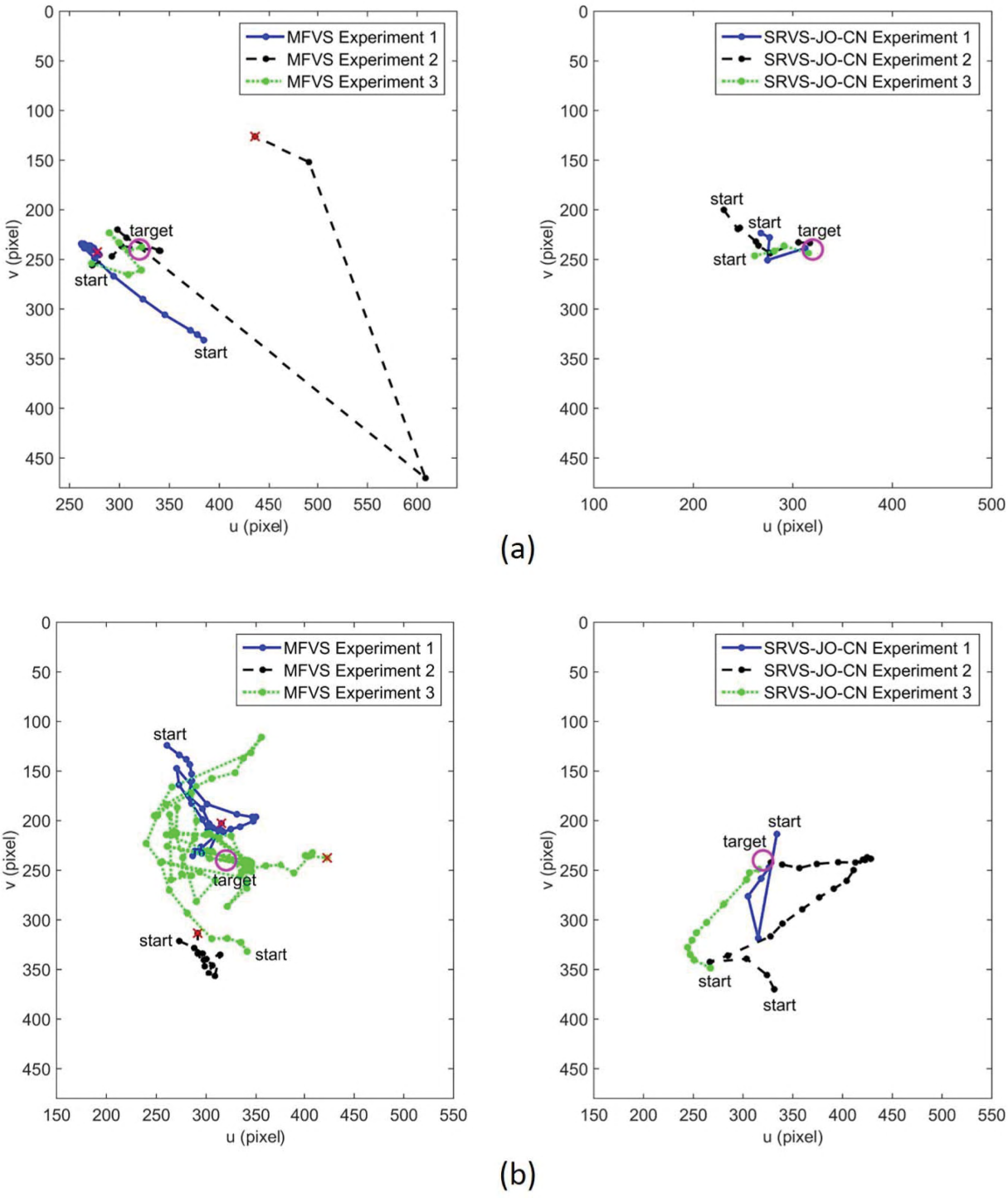

FIGURE 18. Recorded trajectories to evaluate singularity-avoidance effectiveness on the image plane during the visual servoing processes. The start position of the surgical site is indicated and the desired region for the surgical site to be moved in is represented using a magenta circle. An unsuccessful trial due to singularity is distinguished using a red cross. (a) Trajectories recorded during transoral procedures. (b) Trajectories recorded during transnasal procedures. Only the figures on the left have red crosses, because the MFVS experiments were unable to avoid singularity configurations.

this situation. The first one is to add a force sensor at the back of the concentric tube to detect the contact force when the end-effector engages the surface of the target tissue. The approaching process will be terminated once the contact force reaches a threshold value. However, if no contact is allowed in this application, an image based depth estimation

method can be applied as a substitute. After camera calibration, the target depth can be roughly estimated by a pinhole model. In a pinhole model, the image region gets larger in sight when the camera gets closer to target, and gets smaller as the depth increases. Hence, following the similar procedures provided in [47], the depth information can be obtained by the CTR system. Moreover, our proposed visual servoing algorithms SRVS-JO-CND and SRVS-JO-CN can be used even if the robot is approaching the target, due to their singularity-resistant properties. The sophisticated motion planning regarding 3D configuration will be addressed in our future works.

B. LIMITATION OF MULTI-CHANNEL VISUALIZATION AND HYBRID VISUAL-MOTOR CONTROL

Before the cadaveric study, pre-operative computed tomography (CT) images of the cadaver head was collected for visualizing the structure of the respiratory tract and for surgical planning. Intraoperatively, there was limited space for multiple standalone channels of image feedback, so it was difficult to provide a stereo-vision of the respiratory tract during the cadaveric study. It would be beneficial if the respiratory tract could be visualized together with the manipulator end-effector within the same field-of-view intraoperatively, which will be possible when the entire multi-channel system is more miniaturized in the future. We have another independent research project building up a tri-channel concentric tube robot for more comprehensive visualization and bi-manual manipulation within confined spaces [48]. With future multi-channel multi-angle image feedback, the system will be depth-aware. More significantly, this will enable hybrid eye-to-hand and eye-in-hand visual-motor control, which can compensate with each other for better feature tracking: the eye-to-hand configuration using standalone endoscope camera for global coarse positioning to avoid local minimum, and the eye-in-hand configuration as in this manuscript using a hand-mounted endoscope for fine targeting.

C. LIMITATIONS: IMAGE-SPACE SINGLE FEATURE AND SQUARED PIXEL

Though multiple image processing approaches are developed to identify the marker points in image space (by the laser pointer/fiber in our experiments), the proposed singularly avoidance approach uses single image feature point to update the Jacobian, which is sensitive to noisy environment lights. Multiple image feature points or more comprehensive features such as lines, regions or corners can make the visual-motor mapping more resistant from a singular configuration. As a result, this helps avoid projecting artificial markers, which is occupying the limited space inside the human body.

In addition, the proposed uncalibrated image-based visual-motor mapping approach has the assumption that the image space has isotropic squared pixel sizes. However, endoscopic cameras are typically associated with large distortions and small object distance, which may result in the distorted projection for the overall visual-motor Jacobian, especially when images are around different view angles.

D. LIMITATIONS: LOCAL OPTIMUM AND SENSITIVE TO INITIAL CTR-TARGET POSTURE

As seen in Figure 12(b), the SRVS-JO-CND visual-motor control strategy can be trapped in a local optimal region. In this case, we can finely tune the weights between the primary targeting objective and secondary singularity-avoidance, the objective in Eq. (19) or incorporate another standalone camera as mentioned above. Though the visual-motor Jacobian matrix is updated online iteratively and less sensitive to Jacobian initialization, it is sensitive to the initial CTR base positioning. This is because that the curvature design of concentric tubes is dedicated to specific procedures and workspace, where, for example, a transnasal procedure expects the robots entering the workspace through the specific nostril entry with a certain range of entering orientation. If the CTR base is initially too far away from the designed entry posture, the robot can drive to local optimum or singular region.

E. LIMITATION IN PATIENT-SPECIFIC WORK-SPACE

Furthermore, according to our best knowledge, there is no standard way to define the confined working space since the dimensions of pharyngeal vary from one individual to another. Though geometrical constraints could be acquired from preoperative imaging modalities such as MRI or CT for robot motion planning, this would be beyond our focus of intraoperative motion control in this manuscript. In addition, the complicated geometrical modeling process will increase the preparation time and operation costs. In this manuscript, we focus on an intraoperative motion control algorithm for working in confined spaces in general, rather than for a specific patient.

F. LIMITATION IN TASK-SPACE MOTION OPTIMIZATION

The overall Jacobian has differential kinematic mapping directly from actuator space q to the image space (u, v), while ignoring the posture trajectory optimization of end-effector mounted on the endoscope. On the one hand, this gave us the benefit and simplicity of direct visual-actuator mapping by observing the overall Jacobian with respect to the image space without worrying about the Cartesian posture or velocity of the endoscope. On the other hand, the trajectories produced in the image space look smooth and well regulated (close to a straight line in Figure 12(a)) from starting point to the goal position and do not imply the smoothness or continuity of the end-effector motion in the Cartesian space or motor motion in the actuator space (Figure 8 and Figure 9). Instead, the motion trajectory in terms of position and orientation of the endoscope camera attached to the inner-tube end-effector can be contorted.

VIII. CONCLUSION

This paper demonstrated a novel singularity-avoidance model-free eye-in-hand visual servoing technique for continuum tubular robots to achieve safe and reliable control based on image feedback in confined surgical environments. The significance of the proposed algorithm is revealed through high safety requirements during surgical procedures. Moreover, the proposed visual servoing algorithm requires no prior knowledge of the kinematic model of the robot or hand-eye calibration between robot and endoscope. Generally, the proposed visual servoing algorithm adopts a model-free visual servoing framework where the control of the robot and the Jacobian estimation procedure are implemented iteratively until the task is fulfilled. During the iterative process, the estimated Jacobian is optimized when the change in condition number exceeds a predefined threshold. The effectiveness and superiority of the proposed singularity-avoidance model-free visual servoing algorithm are confirmed by simulations and experiments in confined mock-up environments and cadaveric studies.

In the future, the execution time of the singularity-avoidance model-free visual servoing algorithm will be reduced by decreasing the response time of the robot. Meanwhile, considering the live surgical environment, where the patient's body cannot be perfectly immobilized, more sophisticated techniques such as Kalman filtering or motion predicted controller should be used to compensate for undesirable disturbances. Additionally, stereo vision systems will be developed to acquire depth information during the visual servoing process so as to control the robot in a more accurate and appropriate way.

APPENDIX

Stability analysis: Given $\mathbf{x}_d$ is the desired position of the marker, $\mathbf{x}_k$ is the current position of the marker, the error is defined as:

$$\mathbf{e}_\mathbf{x} = \mathbf{x}_d - \mathbf{x}_k \tag{29}$$

The change in error is:

$$\dot{\mathbf{e}}_\mathbf{x} = \dot{\mathbf{x}}_d - \dot{\mathbf{x}}_k \tag{30}$$

Then the Lyapunov function is defined as:

$$V(\mathbf{e}_\mathbf{x}) = \frac{1}{2}\mathbf{e}_\mathbf{x}^\mathrm{T}\mathbf{e}_\mathbf{x} \tag{31}$$

Its derivative is derived as:

$$\begin{aligned}\dot{V}(\mathbf{e}_\mathbf{x}) &= \mathbf{e}_\mathbf{x}^\mathrm{T}\dot{\mathbf{e}}_\mathbf{x} \\ &= \mathbf{e}_\mathbf{x}^\mathrm{T}(\dot{\mathbf{x}}_d - \dot{\mathbf{x}}_k) \\ &= \mathbf{e}_\mathbf{x}^\mathrm{T}\dot{\mathbf{x}}_d - \mathbf{e}_\mathbf{x}^\mathrm{T}\dot{\mathbf{x}}_k\end{aligned} \tag{32}$$

Given a proportional gain closed-loop controller, the desired displacement is described as:

$$\Delta\mathbf{x} = \mathbf{K}_\mathbf{x}(\mathbf{x}_r - \mathbf{x}) \tag{33}$$

where $\mathbf{x}_r$ is the reference position, $\mathbf{K}_\mathbf{x}$ is the positive proportional gain.

Therefore,

$$\dot{V}(\mathbf{e}_\mathbf{x}) = \mathbf{e}_\mathbf{x}^\mathrm{T}\dot{\mathbf{x}}_d - \mathbf{e}_\mathbf{x}^\mathrm{T}\mathbf{K}_\mathbf{x}\mathbf{e}_\mathbf{x} \tag{34}$$

During position regulation, where $\dot{\mathbf{x}}_d = \mathbf{0}$,

$$\dot{V}(\mathbf{e}_\mathbf{x}) = -\mathbf{e}_\mathbf{x}^\mathrm{T}\mathbf{K}_\mathbf{x}\mathbf{e}_\mathbf{x} \tag{35}$$

Then $\dot{V}(\mathbf{e}_\mathbf{x}) < 0$ can be concluded for asymptotic stability.

ACKNOWLEDGMENT

The authors would like to thank Abigail Martin and William Hartley for their proofreading of the manuscript. S. Song was with the Department of Biomedical Engineering, National University of Singapore, Singapore 119077.

REFERENCES

[1] C. Bergeles, A. H. Gosline, N. V. Vasilyev, P. J. Codd, P. J. del Nido, and P. E. Dupont, "Concentric tube robot design and optimization based on task and anatomical constraints," *IEEE Trans. Robot.*, vol. 31, no. 1, pp. 67–84, Feb. 2015.

[2] P. Dupont *et al.*, "Concentric tube robots for minimally invasive surgery," in *Proc. Hamlyn Symp. Med. Robot.*, vol. 7, 2012, p. 8.

[3] P. E. Dupont, J. Lock, B. Itkowitz, and E. Butler, "Design and control of concentric-tube robots," *IEEE Trans. Robot.*, vol. 26, no. 2, pp. 209–225, Apr. 2010.

[4] H. Ren *et al.*, "Computer-assisted transoral surgery with flexible robotics and navigation technologies: A review of recent progress and research challenges," *Crit. Rev. Biomed. Eng.*, vol. 41, nos. 4–5, pp. 365–391, 2013.

[5] P. Marks, "Shape-shifting 'tube robot' could aid heart surgery," *New Sci.*, vol. 206, no. 2761, p. 24, 2010.

[6] Y. Zhou, H. Ren, M. Q.-H. Meng, Z. T. H. Tse, and H. Yu, "Robotics in natural orifice transluminal endoscopic surgery," *J. Mech. Med. Biol.*, vol. 13, no. 2, 2013, Art. no. 1350044.

[7] J. Burgner *et al.*, "A telerobotic system for transnasal surgery," *IEEE/ASME Trans. Mechatronics*, vol. 19, no. 3, pp. 996–1006, Jun. 2014.

[8] H. Ren and P. E. Dupont, "Tubular structure enhancement for surgical instrument detection in 3D ultrasound," in *Proc. Annu. Int. Conf. IEEE Eng. Med. Biol. Soc. (EMBC)*, Aug. 2011, pp. 7203–7206.

[9] E. J. Lobaton, J. Fu, L. G. Torres, and R. Alterovitz, "Continuous shape estimation of continuum robots using X-ray images," in *Proc. IEEE Int. Conf. Robot. Autom. (ICRA)*, May 2013, pp. 725–732.

[10] H. Su *et al.*, "A MRI-guided concentric tube continuum robot with piezoelectric actuation: A feasibility study," in *Proc. IEEE Int. Conf. Robot. Autom. (ICRA)*, May 2012, pp. 1939–1945.

[11] R. A. Lathrop, D. C. Rucker, and R. J. Webster, "Guidance of a steerable cannula robot in soft tissue using preoperative imaging and conoscopic surface contour sensing," in *Proc. IEEE Int. Conf. Robot. Autom. (ICRA)*, May 2010, pp. 5601–5606.

[12] J. Burgner, S. D. Herrell, and R. J. Webster, "Toward fluoroscopic shape reconstruction for control of steerable medical devices," in *Proc. ASME Dyn. Syst. Control Conf. Bath/ASME Symp. Fluid Power Motion Control*, 2011, pp. 791–794.

[13] J. M. Croom, D. C. Rucker, J. M. Romano, and R. J. Webster, "Visual sensing of continuum robot shape using self-organizing maps," in *Proc. IEEE Int. Conf. Robot. Autom. (ICRA)*, May 2010, pp. 4591–4596.

[14] W. Liu, H. Ren, W. Zhang, and S. Song, "Cognitive tracking of surgical instruments based on stereo vision and depth sensing," in *Proc. IEEE Int. Conf. Robot. Biomimetics (ROBIO)*, Dec. 2013, pp. 316–321.

[15] H. Ren, W. Liu, and A. Lim, "Marker-based instrument tracking using dual Kinect sensors for navigated surgery," *IEEE Trans. Autom. Sci. Eng.*, vol. 11, no. 3, pp. 921–924, Jul. 2014.

[16] R. Xu, A. Asadian, A. S. Naidu, and R. V. Patel, "Position control of concentric-tube continuum robots using a modified Jacobian-based approach," in *Proc. IEEE Int. Conf. Robot. Autom. (ICRA)*, May 2013, pp. 5813–5818.

[17] S. Song, Z. Li, H. Yu, and H. Ren, "Electromagnetic positioning for tip tracking and shape sensing of flexible robots," *IEEE Sensors J.*, vol. 15, no. 8, pp. 4565–4575, Aug. 2015.

[18] D. Xu, Y. F. Li, Y. Shen, and M. Tan, "New pose-detection method for self-calibrated cameras based on parallel lines and its application in visual control system," *IEEE Trans. Syst., Man, Cybern. B, Cybern.*, vol. 36, no. 5, pp. 1104–1117, Oct. 2006.
[19] P. Jiang and R. Unbehauen, "Robot visual servoing with iterative learning control," *IEEE Trans. Syst., Man, Cybern. A, Syst. Humans*, vol. 32, no. 2, pp. 281–287, Mar. 2002.
[20] W. Gao, W. Liang, and K. K. Tan, "Alignment motion control for an automated human ear surgery via vision-servoing," *Asian J. Control*, vol. 19, no. 2, pp. 482–493, 2017.
[21] F. Bensalah and F. Chaumette, "Compensation of abrupt motion changes in target tracking by visual servoing," in *Proc. IEEE/RSJ Int. Conf. Intell. Robots Syst. Human Robot Interact. Cooperat. Robots*, vol. 1, Aug. 1995, pp. 181–187.
[22] L. Ott, P. Zanne, F. Nageotte, M. de Mathelin, and J. Gangloff, "Physiological motion rejection in flexible endoscopy using visual servoing," in *Proc. IEEE Int. Conf. Robot. Autom. (ICRA)*, May 2008, pp. 2928–2933.
[23] R. J. Webster, III, J. P. Swensen, J. M. Romano, and N. J. Cowan, "Closed-form differential kinematics for concentric-tube continuum robots with application to visual servoing," in *Experimental Robotics*. Berlin, Germany: Springer, 2009, pp. 485–494.
[24] Y.-H. Liu, H. Wang, C. Wang, and K. K. Lam, "Uncalibrated visual servoing of robots using a depth-independent interaction matrix," *IEEE Trans. Robot.*, vol. 22, no. 4, pp. 804–817, Aug. 2006.
[25] C. Colombo and B. Allotta, "Image-based robot task planning and control using a compact visual representation," *IEEE Trans. Syst., Man, Cybern. A, Syst. Humans*, vol. 29, no. 1, pp. 92–100, Jan. 1999.
[26] H. Wang, W. Chen, X. Yu, T. Deng, X. Wang, and R. Pfeifer, "Visual servo control of cable-driven soft robotic manipulator," in *Proc. IEEE/RSJ Int. Conf. Intell. Robots Syst. (IROS)*, Nov. 2013, pp. 57–62.
[27] H. Wang, W. Chen, C. Wang, X. Wang, and R. Pfeifer, "Dynamic modeling and image-based adaptive visual servoing of cable-driven soft robotic manipulator," *IFAC Proc. Volumes*, vol. 47, no. 3, pp. 11884–11889, 2014.
[28] J. Wang, L. Wu, M. Q.-H. Meng, and H. Ren, "Towards simultaneous coordinate calibrations for cooperative multiple robots," in *Proc. IEEE/RSJ Int. Conf. Intell. Robots Syst. (IROS)*, Sep. 2014, pp. 410–415.
[29] J. Wang, H. Ren, and M. Meng, "Towards occlusion-free surgical instrument tracking: A modular monocular approach and an agile calibration method," *IEEE Trans. Autom. Sci. Eng.*, vol. 12, no. 2, pp. 588–595, Apr. 2015. doi: 10.1109/TASE.2015.2388537.
[30] L. Wu, X. Yang, K. Chen, and H. Ren, "A minimal poe-based model for robotic kinematic calibration with only position measurements," *IEEE Trans. Autom. Sci. Eng.*, vol. 12, no. 2, pp. 758–763, Apr. 2015.
[31] M. C. Yip and D. B. Camarillo, "Model-less feedback control of continuum manipulators in constrained environments," *IEEE Trans. Robot.*, vol. 30, no. 4, pp. 880–889, Aug. 2014.
[32] K. Wu, L. Wu, and H. Ren, "An image based targeting method to guide a tentacle-like curvilinear concentric tube robot," in *Proc. IEEE Int. Conf. Robot. Biomimetics (ROBIO)*, Dec. 2014, pp. 386–391.
[33] K. Wu, L. Wu, C. M. Lim, and H. Ren, "Model-free image guidance for intelligent tubular robots with pre-clinical feasibility study: Towards minimally invasive trans-orifice surgery," in *Proc. IEEE Int. Conf. Inf. Automat.*, Aug. 2015, pp. 749–754.
[34] P. Jiang, L. C. A. Bamforth, Z. Feng, J. E. Baruch, and Y. Chen, "Indirect iterative learning control for a discrete visual servo without a camera-robot model," *IEEE Trans. Syst., Man, Cybern. B, Cybern.*, vol. 37, no. 4, pp. 863–876, Aug. 2007.
[35] T. Yoshikawa, "Manipulability of robotic mechanisms," *Int. J. Robot. Res.*, vol. 4, no. 2, pp. 3–9, 1985.
[36] M. Shahamiri and M. Jagersand, "Uncalibrated visual servoing using a biased newton method for on-line singularity detection and avoidance," in *Proc. IEEE/RSJ Int. Conf. Intell. Robots Syst.*, Aug. 2015, pp. 3953–3958.
[37] W. Zhu, S. Liang, Y. Wei, and J. Sun, "Saliency optimization from robust background detection," in *Proc. IEEE Conf. Comput. Vis. Pattern Recognit. (CVPR)*, Jun. 2014, pp. 2814–2821.
[38] C. Yang, L. Zhan, H. Lu, X. Ruan, and M.-H. Yang, "Saliency detection via graph-based manifold ranking," in *Proc. IEEE Conf. Comput. Vis. Pattern Recognit. (CVPR)*, Jun. 2013, pp. 3166–3173.
[39] J.-C. Guo, Z. Liu, and G.-Z. Cui, "Modelling and optimization approach for trajectory planning of three freedom planar manipulators," *J. Pure Appl. Math., Adv. Appl.*, vol. 7, no. 1, pp. 1–20, 2012.
[40] F. Chaumette, "Potential problems of stability and convergence in image-based and position-based visual servoing," in *The Confluence of Vision and Control*. Berlin, Germany: Springer, 1998, pp. 66–78.
[41] S. Sen, B. Dasgupta, and A. K. Mallik, "Variational approach for singularity-free path-planning of parallel manipulators," *Mech. Mach. Theory*, vol. 38, no. 11, pp. 1165–1183, 2003.
[42] C. M. Gosselin and J. Angeles, "The optimum kinematic design of a spherical three-degree-of-freedom parallel manipulator," *J. Mech., Transmiss., Automat. Des.*, vol. 111, no. 2, pp. 202–207, 1989.
[43] B. Siciliano, "Kinematic control of redundant robot manipulators: A tutorial," *J. Intell. Robot. Syst.*, vol. 3, no. 3, pp. 201–212, Sep. 1990.
[44] S. Song *et al.*, "6-D magnetic localization and orientation method for an annular magnet based on a closed-form analytical model," *IEEE Trans. Magn.*, vol. 50, no. 9, Sep. 2014, Art. no. 5000411.
[45] J. Kennedy and R. Eberhart, "Particle swarm optimization," in *Proc. IEEE Int. Conf. Neural Netw.*, Nov./Dec. 1995, pp. 1942–1948.
[46] L. Wu, S. Song, K. Wu, C. M. Lin, and H. Ren, "Development of a compact continuum tubular robotic system for nasopharyngeal biopsy," *Med. Biol. Eng. Comput.*, vol. 55, no. 3, pp. 403–417, 2017, doi: 10.1007/s11517-016-1514-9.
[47] A. Torralba and A. Oliva, "Depth estimation from image structure," *IEEE Trans. Pattern Anal. Mach. Intell.*, vol. 24, no. 9, pp. 1226–1238, Sep. 2002.
[48] H. Yu, L. Wu, K. Wu, and H. Ren, "Development of a multi-channel concentric tube robotic system with active vision for transnasal nasopharyngeal carcinoma procedures," *IEEE Robot. Autom. Lett.*, vol. 1, no. 2, pp. 1172–1178, Jul. 2016.

KEYU WU received the B.S. degree in bioengineering from the National University of Singapore, in 2013, where she is currently pursuing the Ph.D. degree with the Department of Biomedical Engineering. Her research interests mainly include visual servoing and motion planning for flexible surgical robots and statistical atlas construction for implant and robot design.

GUONIU ZHU received the B.Sc. degree in mechanical engineering and automation from the China University of Mining and Technology, in 2008, the M.Sc. degree in mechanical design and theory from the Hefei University of Technology, in 2011, and the Ph.D. degree, in 2017. After that, he was with Minmetals Mining (Anhui) Development Co. Ltd., from 2011 to 2012. He is currently pursuing the Ph.D. degree with the State Key Laboratory of Mechanical System and Vibration, School of Mechanical Engineering, Shanghai Jiao Tong University, which is the top ranked university in China. He is a Research Fellow with the National University of Singapore.

LIAO WU received the B.S. and Ph.D. degrees in mechanical engineering from Tsinghua University, Beijing, China, in 2008 and 2013, respectively. From 2013 to 2015, he was a Research Fellow with the Department of Biomedical Engineering, National University of Singapore. Since 2016, he has been a Vice Chancellor's Research Fellow with the Australian Centre for Robotic Vision, Queensland University of Technology, Brisbane, Australia. His research mainly focuses on medical robotics and industrial robotics. He is interested in fundamental theories such as kinematics, calibration, and application of Lie group theory in robotics. His research interest also includes engineering techniques for the development of mechatronic systems.

WENCHAO GAO received the Ph.D. degree from the Graduate School for Integrative Sciences and Engineering, National University of Singapore, and the B.Eng. degree from the National University of Singapore. He was a Research Fellow with the BME Department, National University of Singapore. His research interests are in the area of medical devices and applications.

SHUANG SONG received the B.S. degree in computer science and technology from North Power Electric University, Baoding, the M.S. degrees in computer architecture from the Chinese Academy of Sciences, and the Ph.D. degree in computer application technology from the University of Chinese Academy of Sciences, China, in 2007, 2010, and 2013, respectively. He was a Research Fellow with the Department of Biomedical Engineering, National University of Singapore. He is currently an Assistant Professor with the School of Mechanical Engineering and Automation, Harbin Institute of Technology Shenzhen Graduate School, Shenzhen, China. His research interests include magnetic tracking and actuation method for bioengineering applications, such as surgical robots and micromanipulation, mainly focusing on the area of biomedical robotics.

CHWEE MING LIM received the M.B.B.S. degree from the Faculty of Medicine, National University of Singapore (NUS), Singapore, in 1998. He underwent residency in otolaryngology in Singapore. After completing his specialist training, he joined the Department of Otolaryngology-Head and Neck Surgery, National University Health System (NUHS), Singapore, as an Associate Consultant. He is currently a Senior Consultant with the Department of Otolaryngology-Head and Neck Surgery, NUHS, and also an Assistant Professor with the Yong Loo Lin School of Medicine, NUS. His clinical subspecialty is thyroid surgery, robotic-assisted surgery, head and neck surgery, and surgical oncology. He received the Gold Medal for the MRCS (Edinburgh) General Surgery Examination, in 2003. Subsequently, he received the Gold Medal from the College of Surgeons for the Best Performing Resident in the exit examination organized by the Specialist Training Committee in Otolaryngology, in 2009. In 2010, he received the Ministry of Health Overseas Training Award and pursued a two-year Advanced Head and Neck Oncologic Fellowship at the University of Pittsburgh Medical Center, Pittsburgh, PA, USA.

HONGLIANG REN (M'15–SM'17) received the Ph.D. degree in electronic engineering (specialized in biomedical engineering) from The Chinese University of Hong Kong, Hong Kong, in 2008. He was a Research Fellow with Johns Hopkins University, Baltimore, MD, USA; Children's Hospital Boston & Harvard Medical School, Boston, MA, USA; and the Children's National Medical Center, Washington, DC, USA. He is currently an Assistant Professor, and is leading a research group on medical mechatronics with the Biomedical Engineering Department, National University of Singapore (NUS), Singapore. He is also an affiliated Principal Investigator of the Singapore Institute of Neurotechnology; the NUS (Suzhou) Research Institute, Suzhou, China; and the Advanced Robotics Center, NUS. His main areas of interests include biorobotics and intelligent control, medical mechatronics, computer-integrated surgery, and multisensor data fusion in surgical robotics. He is a recipient of the NUS Young Investigator Award, the IAMBE Early Career Award 2018, and the Interstellar Early Career Investigator Award 2018.